

Orbital-scale precipitation variations in Northwest China modulated by equatorial spring insolation

Yunxia Gan, Ziyu Zhou, Xiaojian Zhang^{*}

School of Geography and Ocean Science, Frontiers Science Center for Critical Earth Material Cycling, Nanjing University, Nanjing 210023, China



ARTICLE INFO

Editor: P Srivastava

Keywords:

Climate simulation
Orbital forcing
Holocene
Moisture change
Arid Central Asia

ABSTRACT

The mechanisms underlying orbital-scale precipitation patterns in Northwest China during the Holocene remain incompletely elucidated. In particular, the role of orbital forcing in Holocene precipitation variations in Northwest China is still not very clear. This study aims to investigate the response of precipitation variations in Northwest China to orbital forcing by comparing their behaviors between the Holocene and Last Interglacial (LIG) periods through climate simulations. Simulation results indicate that the mid-Holocene experienced relatively minor drying compared to the early Holocene, while the late Holocene was marked by substantial wetting relative to the mid-Holocene during the summer half-year (April–September) in Northwest China. This simulated evolution pattern exhibits a strong concordance with reconstructions. The increase of precipitation in Northwest China during the Holocene was paced by an elevated spring insolation at the equator. Analogous to the Holocene, precipitation variations in Northwest China during the LIG exhibited a strong coherence with equatorial spring insolation. The increase in equatorial spring insolation induced a persistent warming in the Indo-Pacific warm pool (IPWP) during the summer half-year. The IPWP warming forced a southward displacement of the Asian subtropical westerly jet and a westward extension of the western Pacific subtropical high, which together contributed to anomalous upward motions and the subsequent increase in precipitation over Northwest China. Therefore, orbital-scale precipitation variations were significantly affected by spring insolation at the equator.

1. Introduction

Northwest China is geographically located in the heartland of Eurasia, far away from any ocean, resulting in significantly low levels of atmospheric humidity (Chen et al., 2021; Zhang, 2021). In addition, Northwest China is prevailing with persistent subsidence induced by the thermal effect of the Tibetan Plateau (Sato and Kimura, 2005; Wu et al., 2015; Sun and Liu, 2021). The combination of these two factors results in an extremely arid climate in Northwest China (Yang et al., 2023). The environmental dynamics (e.g., ecosystem, glacier, and hydrology) and societal transformations exhibit a high degree of sensitivity to precipitation fluctuations within this region (Chen et al., 2019; Zhang et al., 2022a). Therefore, it is imperative to acquire a more profound comprehension of the physical mechanisms underlying precipitation variations in Northwest China at different timescales.

The precipitation variations in Northwest China during the Holocene have been extensively reconstructed utilizing multiple proxies (Cheng et al., 2012; Wang and Feng, 2013; Chen et al., 2016). These

reconstructions demonstrate distinct evolutionary patterns of precipitation changes in Northwest China throughout the Holocene (Zhang et al., 2017; Chen et al., 2022). Some reconstructions, such as stalagmite $\delta^{18}\text{O}$ records, indicate an increasing trend of precipitation since the early Holocene in this region, which was consistent with that recorded in the Asian monsoon region (Cheng et al., 2012; Cai et al., 2017). The majority of the records indicate a significantly higher precipitation regime during the late Holocene in Northwest China, contrasting with the relatively weaker Asian summer monsoon (ASM) (Wang and Feng, 2013; Chen et al., 2019, 2022; Xu et al., 2019; Lan et al., 2021; Zhang, 2021). Moreover, the stalagmite trace-element records also exhibit concordance with the climatic pattern of heightened precipitation during the late Holocene in Northwest China, thereby challenging the notion that stalagmite $\delta^{18}\text{O}$ serves as a reliable proxy for precipitation amount in Northwest China (Liu et al., 2020). The stalagmite $\delta^{18}\text{O}$ in Northwest China is proposed to serve as an indicator of the moisture source (Zhang and Jin, 2016; Zhang, 2021; Chen et al., 2022).

Changes of precipitation in Northwest China are primarily

* Corresponding author.

E-mail address: zhangxj@nju.edu.cn (X. Zhang).

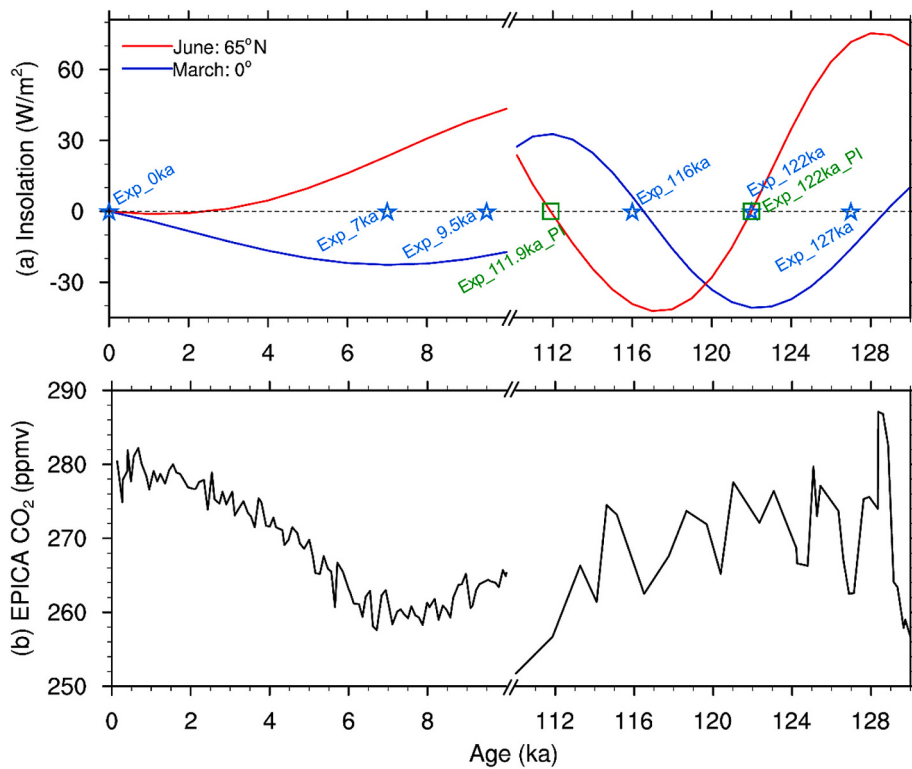


Fig. 1. Changes in June insolation (Laskar et al., 2004) at 65° N (red line) and March insolation at 0° relative to the PI (a), and CO₂ concentration (Lüthi et al., 2008) (b). The time slices simulated in this study are marked by blue stars and green rectangles. (For interpretation of the references to colour in this figure legend, the reader is referred to the web version of this article.)

Table 1
Boundary conditions used in the climate simulations.

	Exp_0ka	Exp_7ka	Exp_9.5ka	Exp_116ka	Exp_122ka	Exp_127ka	Exp_111.9ka_PI	Exp_122ka_PI
Eccentricity	0.016764	0.01891061	0.01935327	0.04140942	0.04074438	0.0397793	0.04128599	0.04074438
Obliquity	23.459	24.16736	24.23109	22.48753	23.33631	24.04015	22.31779	23.33631
Perihelion-180°	100.33	344.2766	303.0330	94.17360	355.3651	275.4082	162.8314	355.3651
CO ₂ (ppmv)	284.3	260.203	263.776	266.376	273.526	262.546	PI (0 ka BP)	PI
CH ₄ (ppbv)	808.2	614.020	676.831	496.685	608.505	646.690	PI	PI
N ₂ O (ppbv)	273.0	259.626	260.637	254.663	258.933	254.334	PI	PI
Topography/coastlines	PI							
Ice sheets	PI							

Table 2
Summary of 9 proxy records used in this study.

No.	Site name	Lat.	Lon.	Proxy type	Dating method	Number of dates	References
1	Lake Aibi	44.95° N	82.75° E	Pollen	AMS ¹⁴ C	6	Wang et al., 2013
2	Baluk Cave	42.43° N	84.73° E	Sr/Ca	U-Th	48	Liu et al., 2020
3	Lujiaowan Section	43.98° N	85.33° E	Magnetic susceptibility	OSL, AMS ¹⁴ C	15	Chen et al., 2016
4	Zeketai Section	43.50° N	93.32° E	Magnetic susceptibility	OSL, AMS ¹⁴ C	11	Jia et al., 2021
5	Chaiwopu Peat	43.48° N	87.93° E	$\delta^{13}\text{C}$	AMS ¹⁴ C	13	Hong et al., 2014
6	Lake Wulungu	47.20° N	87.30° E	Pollen	AMS ¹⁴ C	6	Liu et al., 2008
7	Core SO188-17286-1	19.74° N	89.88° E	U_{37}^{K}	AMS ¹⁴ C	3	Wang et al., 2022
8	Core RC12-344	12.46° N	96.04° E	Mg/Ca	AMS ¹⁴ C	4	Rashid et al., 2007
9	Core SO139-74KL	6.54° S	103.83° E	U_{37}^{K}	AMS ¹⁴ C	5	Lücke et al., 2009

influenced by moisture transports (Chen et al., 2021; Zhang, 2021). The moisture responsible for precipitation in Northwest China is mainly transported by the westerlies from the North Atlantic, the Mediterranean and Caspian seas, as well as by the monsoonal easterlies from the tropical Indian Ocean and Northwest Pacific (Jin et al., 2012; Chen et al., 2021; Shi et al., 2021; Zhang, 2021). The strength of the westerlies is dominated by the meridional pressure gradient, which arises from the thermal contrast between the low and high latitudes (Jin et al., 2012;

Chen et al., 2016, 2019). The strength of the monsoonal easterlies is associated with the anomalous anticyclone over the Mongolia, which is negatively correlated to the ASM intensity (Chen et al., 2021; Zhang, 2021).

During the Holocene, climate variations were predominantly controlled by changes in insolation induced by Earth's orbital parameters (Laskar et al., 2004; Wanner et al., 2008; Marcott et al., 2013). The thermal contrast between the low and high latitudes was directly

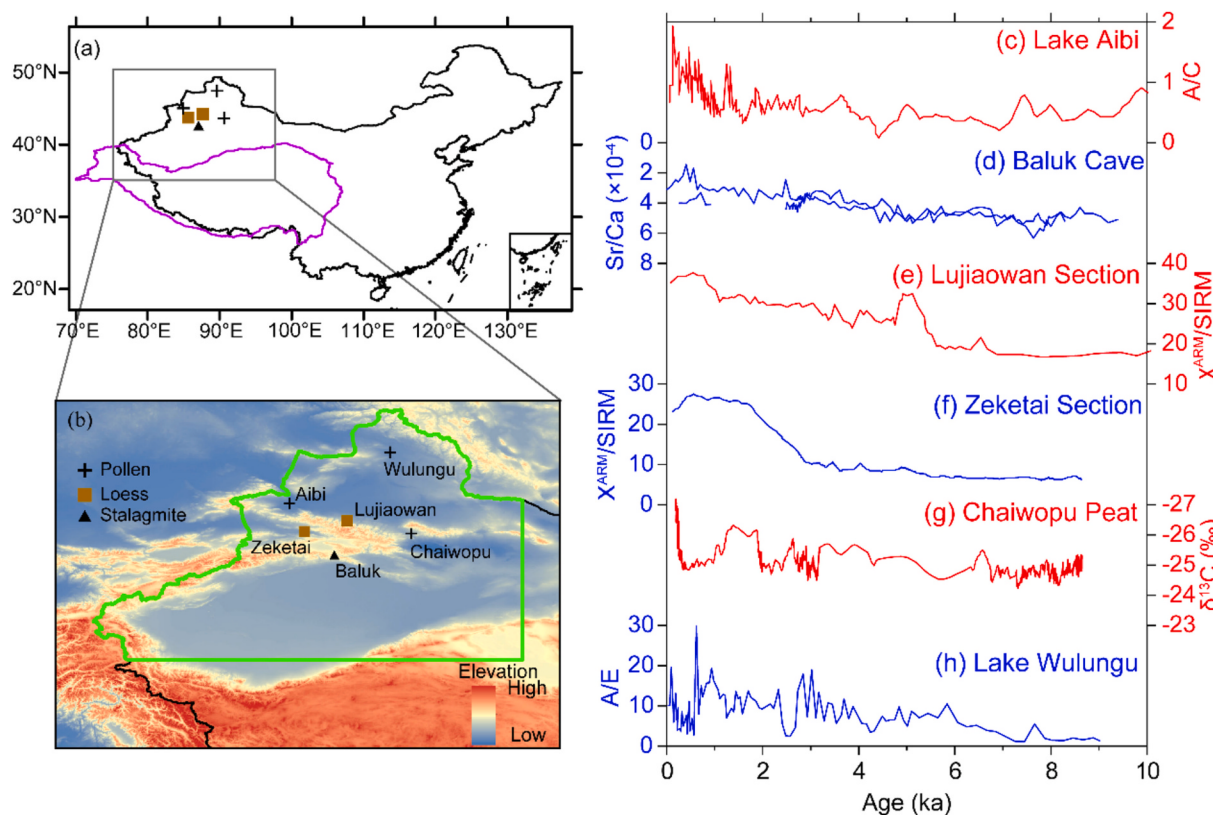


Fig. 2. The geographical locations of the study area (a) and the records employed in this study (b). The study region is outlined by the green contour. Holocene moisture evolution in Northwest China documented by proxy records in Lake Aibi (Wang et al., 2013) (c), Baluk Cave (Liu et al., 2020) (d), Lujiaowan Loess Section (Chen et al., 2016) (e), Zeketai Loess Section (Jia et al., 2021) (f), Chaiwopu Peat (Hong et al., 2014) (g), and Lake Wulungu (Liu et al., 2008) (h). (For interpretation of the references to colour in this figure legend, the reader is referred to the web version of this article.)

associated with the meridional gradient of incoming summer insolation (Davis and Brewer, 2009). That is, the strength of the westerlies was ultimately controlled by orbitally-induced summer insolation changes during the Holocene (Chen et al., 2016, 2019). The amplification of meridional insolation gradient contributed to the establishment of a more humid climate regime in Northwest China during the late Holocene (Chen et al., 2016, 2019, 2022). The evolution of the ASM was also directly controlled by summer insolation during the Holocene (Zhang et al., 2023), which modulated the land-sea thermal contrast between the Eurasia and tropical Indian Ocean/North Pacific (Jiang et al., 2013; Chen et al., 2016). The declining summer insolation led to a weakening of the ASM, resulting in an intensified westward moisture transport during the late Holocene, thereby leading to increased precipitation in Northwest China (Zhang, 2021). Hence, the wetter climate regime in Northwest China during the late Holocene primarily resulted from the interplay between the ASM and mid-latitude westerlies, which was directly influenced by orbital forcing.

It should be noted that the wetting trend of Northwest China predominantly commenced during the mid-Holocene (e.g., Chen et al., 2016; Liu et al., 2020; Lan et al., 2021). Many records reconstruct no significant shift or even a slight drying trend from the early to mid-Holocene in Northwest China, which cannot be attributed to the decline in summer insolation and the amplification in meridional summer insolation gradient (Xu et al., 2019; Lan et al., 2021). The mechanisms underlying the mid-Holocene drought in Northwest China remain inadequately understood (Xu et al., 2019). Contemporary climate studies indicate the significant role of the ocean feedbacks over the tropical Indian Ocean in modulating precipitation variations observed in Northwest China over recent decades (Ding et al., 2022; Wang et al., 2022a; Wu et al., 2022). Mid-Holocene climate simulations have also unveiled the crucial role of the ocean feedbacks across the tropical

Indian Ocean in driving precipitation changes during the mid-Holocene in Northwest China (Yang et al., 2023). The tropical Indian Ocean receives a maximum insolation during the spring season. The ocean feedbacks in the tropical Indian Ocean were likely influenced by changes in spring insolation during the Holocene (Zhang et al., 2024). Therefore, the precipitation variations in Northwest China might be affected by spring insolation during the Holocene.

The orbital parameters of Earth display clearly discernible periodic fluctuations (Berger and Loutre, 1991). Investigating climate variations during periods analogous to the Holocene would enhance our comprehension of the climatic dynamics throughout this epoch. The Last Interglacial (LIG) exhibited comparable orbital forcing patterns to those observed during the Holocene (Bova et al., 2021). Additionally, the LIG experienced an enhanced seasonality in comparison to the Holocene epoch (Bova et al., 2021). Hence, the comparisons between the LIG and Holocene epochs could yield a more profound understanding of how precipitation variations in Northwest China respond to orbital forcing. In this study, we intend to explore the response of precipitation variations in Northwest China to orbital forcing via climate simulations during the LIG and Holocene epochs. We place particular emphasis on the role of equatorial spring insolation in driving precipitation variability in Northwest China.

2. Methods

2.1. Climate simulations

This study employs the Community Earth System Model version 1.2 (CESM1.2; Hurrell et al., 2013), developed by the National Center for Atmospheric Research (NCAR), to investigate the response of precipitation variations in Northwest China to orbital forcing during the

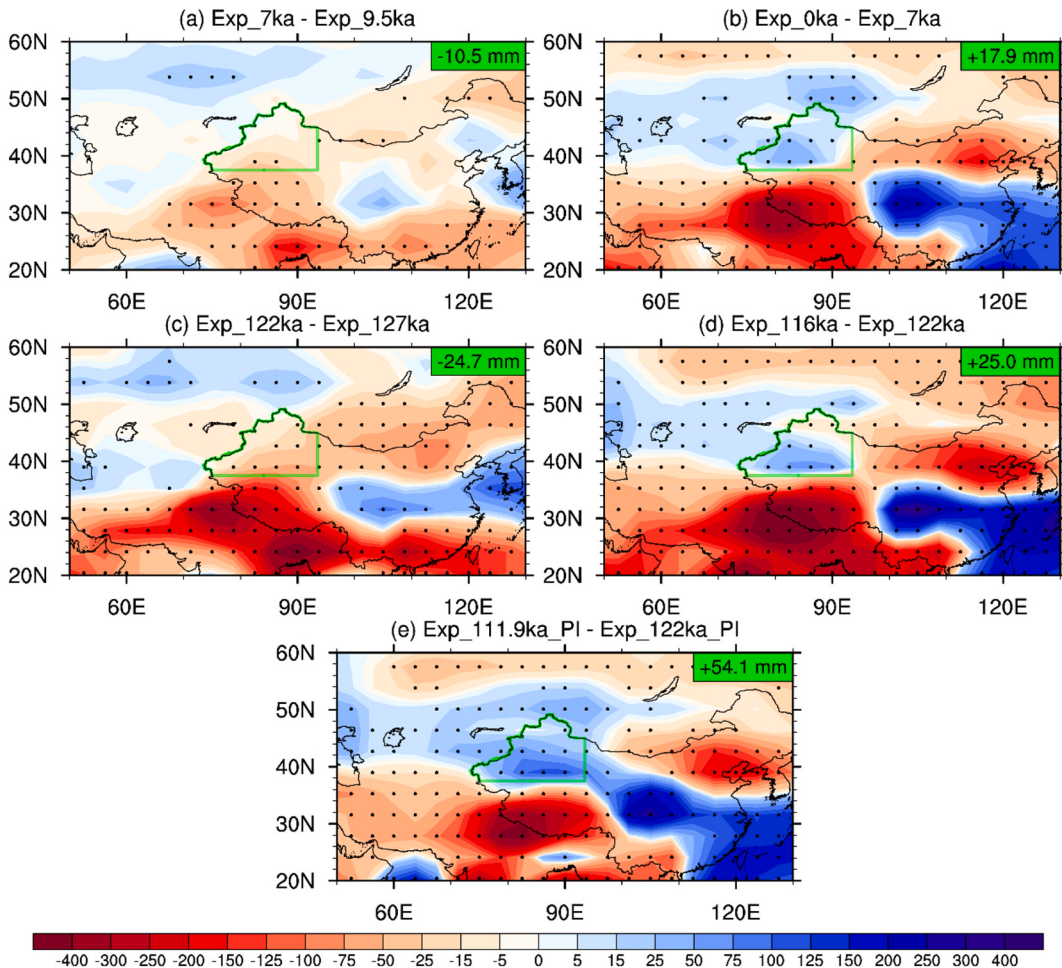


Fig. 3. Composite differences of mean summer half-year precipitation (mm) between Exp_7ka and Exp_9.5ka (a), between Exp_0ka and Exp_7ka (b) during the Holocene, between Exp_122ka and Exp_127ka (c), between Exp_116ka and Exp_122ka (d) during the LIG, as well as between Exp_111.9ka_PI and Exp_122ka_PI (e). Dotted regions indicate differences that are significant at the 0.05 confidence level. The study region is outlined by the green contour. The value in the top-right corner represents the change in area-averaged precipitation over the study region. (For interpretation of the references to colour in this figure legend, the reader is referred to the web version of this article.)

Holocene and LIG epochs. The CESM1.2 is a fully coupled Earth system model that integrates the spectral atmospheric model Community Atmospheric Model version 4 (CAM4; Neale et al., 2013), the land model Community Land Model version 4.0 (CLM4.0; Lawrence et al., 2011), the ocean model Parallel Ocean Program version 2 (POP2; Danabasoglu et al., 2012), and the sea-ice model Community Ice Code version 4.0 (CICE4.0; Hunke and Lipscomb, 2008) through the flux coupler CPL7 (Craig et al., 2012). The CESM 1.2 accommodates diverse spatial and temporal resolutions as well as intricate algorithms. The simulations were conducted using a low-resolution model version (T31_g37). The CAM4 and CLM4.0 models exhibit a horizontal resolution of T31 ($3.75^\circ \times 3.75^\circ$), while the POP2 and CICE4.0 models demonstrate a horizontal resolution of gx3v7, with 100 grid points in the zonal directions and 116 grid points in the meridional direction. The CAM4 has 26 hybrid sigma-pressure levels, while the POP2 has 60 vertical levels.

We performed time-slice simulations at 9.5 ka and 127 ka (Exp_9.5ka and Exp_127ka) to model the climatic response to enhanced boreal summer insolation forcing during the early periods of the Holocene and LIG, respectively (Fig. 1). Time slices at 0 ka and 116 ka (Exp_0ka and Exp_116ka) were simulated to capture the climatic response to decreased boreal summer insolation forcing during the late periods of the Holocene and LIG, respectively. Simulations at 7 ka and 122 ka (Exp_7ka and Exp_122ka) were also performed to model the climatic response to decreased equatorial spring insolation during the middle

periods of the Holocene and LIG, respectively. These six experiments were driven by Earth's orbital parameters (Berger and Loutre, 1991) and greenhouse gas concentrations (Louergue et al., 2008; Lüthi et al., 2008; Schilt et al., 2010). The ice sheets are consistent with the pre-industrial period (PI, 0 ka BP). In addition, we specifically conducted two simulations at 111.9 ka and 122 ka (Exp_111.9ka_PI and Exp_122ka_PI). The Northern Hemisphere experienced comparable insolation levels in June during both periods, similar to the PI era. However, at 111.9 ka, the equator received relatively higher insolation levels in March compared to 122 ka when the opposite was observed (Fig. 1a). These two simulations are exclusively forced by Earth's orbital parameters, while maintaining the same ice sheets and greenhouse gas concentrations as in the PI conditions. The boundary conditions for the above simulations are summarized in Table 1. The simulations were integrated for 2000 model years in order to attain a quasi-equilibrium state. We analyzed the last 100 model years of these simulations to avoid potential model drifts.

2.2. Proxy records

Relevant proxy records in Northwest China were additionally employed for comparative analysis with our simulations during the Holocene. We collected in this study six moisture-related reconstructions that possess reliable chronological control and clear

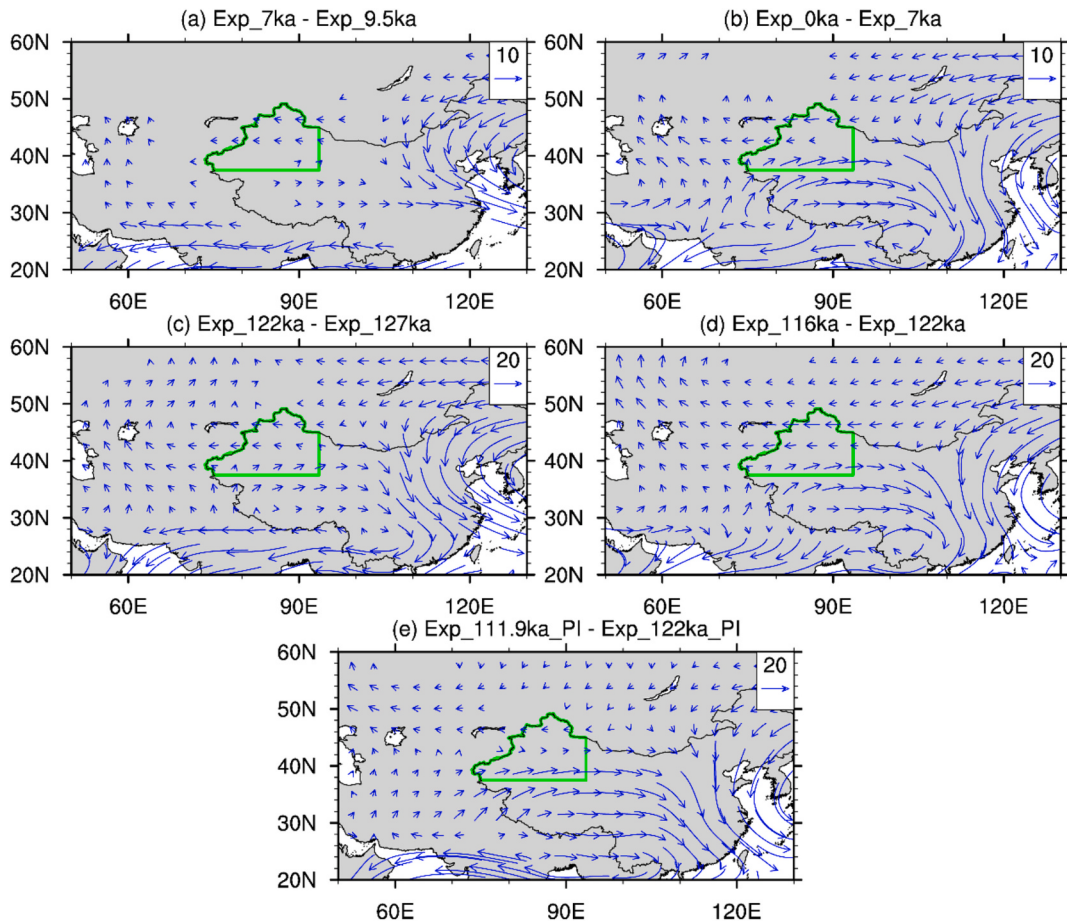


Fig. 4. Composite differences of mean summer half-year water vapor flux ($\text{kg} \cdot \text{m}^{-1} \cdot \text{s}^{-1}$) vertically integrated from the surface to 200 hPa between Exp_7ka and Exp_9.5ka (a), between Exp_0ka and Exp_7ka (b) during the Holocene, between Exp_122ka and Exp_127ka (c), between Exp_116ka and Exp_122ka (d) during the LIG, as well as between Exp_111.9ka_PI and Exp_122ka_PI (e). Only differences exceeding the 0.05 significance level are plotted. The study region is outlined by the green contour. (For interpretation of the references to colour in this figure legend, the reader is referred to the web version of this article.)

climatic significance. The six records include two pollen records (Lake Aibi, and Lake Wulungu), one carbon-isotope record (Chaiwopu Peat), one stalagmite trace-element records (Baluk Cave), two loess magnetic susceptibility (MS) records (Lujiaowan Section, and Zeketai Section). In addition, three Holocene sea surface temperature (SST) records from the Indo-Pacific Warm Pool (IPWP) were utilized for comparison with our simulations, aiming to elucidate the underlying mechanisms driving precipitation variations in Northwest China. The summaries of these records are shown in Table 2.

Precise chronologies serve as the foundation for climatic reconstruction and facilitate model-proxy comparisons. Chronologies of Holocene records primarily rely on Accelerator Mass Spectrometry (AMS) ^{14}C and U—Th methods (Table 2). However, AMS ^{14}C dating exceeds the temporal limit for LIG records. U—Th dating is predominantly utilized in speleothem records, which are limited in availability in Northwest China during the LIG (Cheng et al., 2012). LIG records in Northwest China are predominantly dated using optically stimulated luminescence (OSL) method (Li et al., 2020), which is associated with considerable uncertainties in their chronological frameworks (Galbraith and Roberts, 2012). Therefore, proxy records are not utilized for comparison with the simulations of the LIG, due to the limited availability of records in Northwest China and substantial uncertainties in chronologies.

3. Results

3.1. Model-proxy comparisons

These six proxy records generally indicate a significantly higher precipitation regime in Northwest China during the late Holocene compared to the early and mid-Holocene (Fig. 2). Most of the records indicate no discernible wetting trend in this area during the early to mid-Holocene period. In particular, the pollen record of Lake Aibi reveals a drying trend during the early to mid-Holocene. In general, proxy records consistently depict an increase in moisture levels across Northwest China since approximately 7 ka.

In Northwest China, the majority of precipitation occurs during the summer half-year (April–September) (Yang et al., 2023). The CESM simulations reveal no significant changes in summer half-year precipitation in Northwest China at 7 ka relative to 9.5 ka, with the exception of a pronounced decrease of 15.0–25.0 mm in southern Xinjiang (Fig. 3a). At 0 ka, the simulation results indicate a pronounced increase in summer half-year precipitation by 5.0–50.0 mm in the southern and central parts of Xinjiang, Northwest China, compared to 7 ka (Fig. 3b). The increase in the northern region of Xinjiang, Northwest China, exhibited weak statistical significance. Mid-Holocene precipitation changes in Xinjiang, Northwest China, were out of phase with those in monsoon transitional zone and monsoon-controlled zone in North China (Fig. 3b). In this study, we specifically focus on precipitation changes in Xinjiang, Northwest China, which is approximately outlined by the green contour in Fig. 3b. From the regional average, summer half-year precipitation in

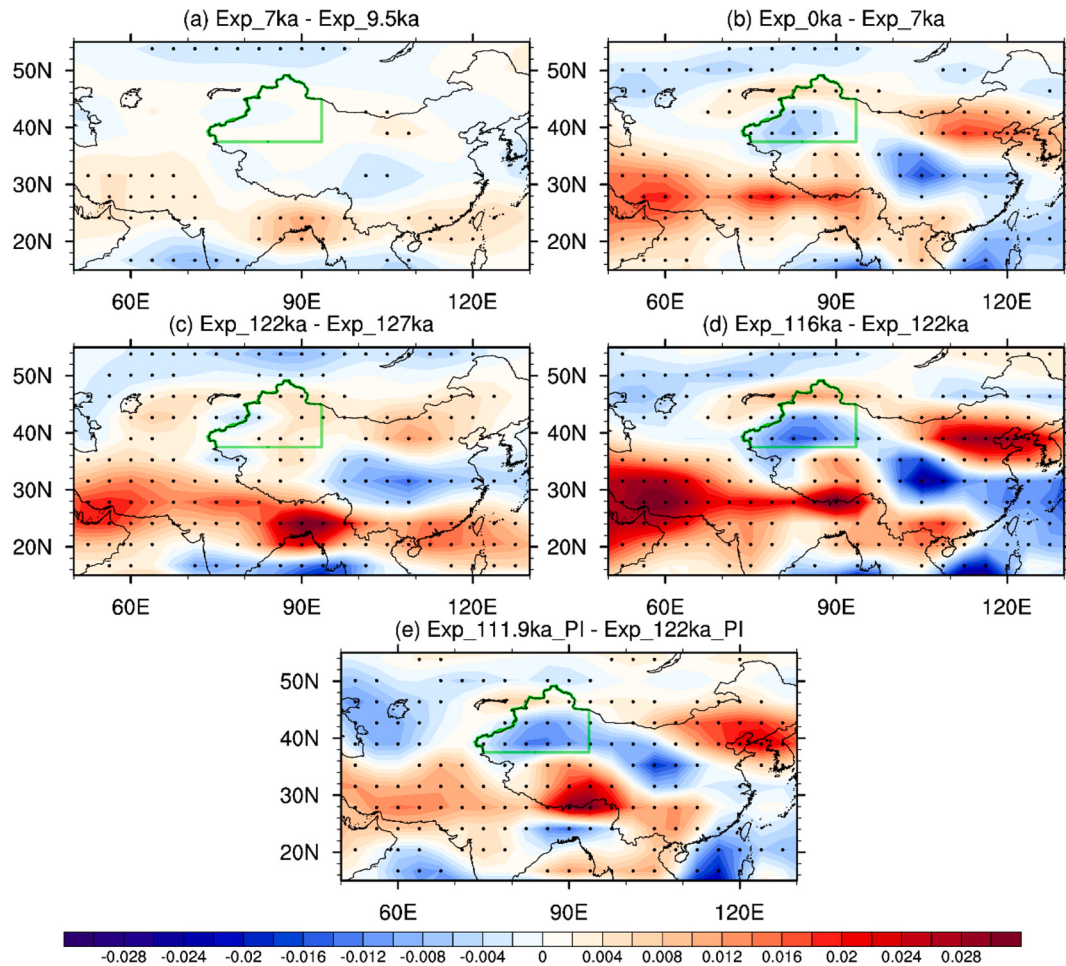


Fig. 5. Composite differences of mean summer half-year vertical velocity ($\text{Pa} \cdot \text{s}^{-1}$) at 500 hPa between Exp_7ka and Exp_9.5ka (a), between Exp_0ka and Exp_7ka (b) during the Holocene, between Exp_122ka and Exp_127ka (c), between Exp_116ka and Exp_122ka (d) during the LIG, as well as between Exp_111.9ka_PI and Exp_122ka_PI (e). Dotted regions indicate differences that are significant at the 0.05 confidence level. The study region is outlined by the green contour. (For interpretation of the references to colour in this figure legend, the reader is referred to the web version of this article.)

the study area decreased by 10.5 mm at 7 ka compared to 9.5 ka, and increased by 17.9 mm at 0 ka relative to 7 ka (Fig. 3a, b). In general, the simulations exhibit a strong agreement with the records regarding the moisture evolution in Northwest China during the Holocene.

The combined evidence from climate simulations and proxy records demonstrates enhanced precipitation in Northwest China during the late Holocene compared to the mid-Holocene (Figs. 2 and 3). This shift coincides with increased spring insolation at the equator and decreased summer insolation in the Northern Hemisphere (Fig. 1). However, the decrease in summer insolation in the Northern Hemisphere was not accompanied by a significant wetting of Northwest China during the mid-Holocene relative to the early Holocene (Figs. 1, 2, and 3). In contrast, the insignificant precipitation variations were associated with a slight decrease in equatorial spring insolation between the mid- and early Holocene. This implies that equatorial spring insolation might play a significant role in driving orbital-scale precipitation variability in Northwest China during the Holocene. The LIG simulations also reveal a reduction of summer half-year precipitation in Northwest China by 24.7 mm at 122 ka compared to 127 ka (Fig. 3c), and an increase of 25.0 mm at 116 ka relative to 122 ka (Fig. 3d). This evolution pattern closely followed changes in equatorial spring insolation during the LIG (Fig. 1b). Hence, the LIG simulations also imply a potential role of equatorial spring insolation in orbital-scale precipitation variations in Northwest China.

It is worth noting that simulations demonstrate a comparable

evolution pattern of precipitation variations in Northwest China between spring and summer for both the Holocene and LIG periods (Figs. S1 and S2). The variations in summer precipitation in Northwest China (Fig. S2) were not fully synchronized with summer insolation, but exhibited a strong association with spring insolation (Fig. 1a). The declining trend of summer insolation alone fails to account for orbital-scale variations in summer precipitation in Northwest China. Equatorial spring insolation might exert a prolonged effect on orbital-scale variations of precipitation in Northwest China in the following summer. Hence, the variations in summer half-year precipitation in Northwest China demonstrated a close association with equatorial spring insolation.

To further validate the potential role of equatorial spring insolation, we compare precipitation variations in Northwest China with analogous summer insolation levels but distinct spring insolation levels (Fig. 1a). The CESM simulations demonstrate a notable increase of 54.1 mm in summer half-year precipitation in Northwest China at 111.9 ka compared to 122 ka (Fig. 3e), which was linked to a substantial rise in equatorial spring insolation (Fig. 1a). This significant increase in precipitation is simulated not only during spring (29.3 mm; Fig. S1e) but also throughout summer (24.8 mm; Fig. S2e). Therefore, it is highly probable that equatorial spring insolation exerts a modulating influence on orbital-scale precipitation variations.

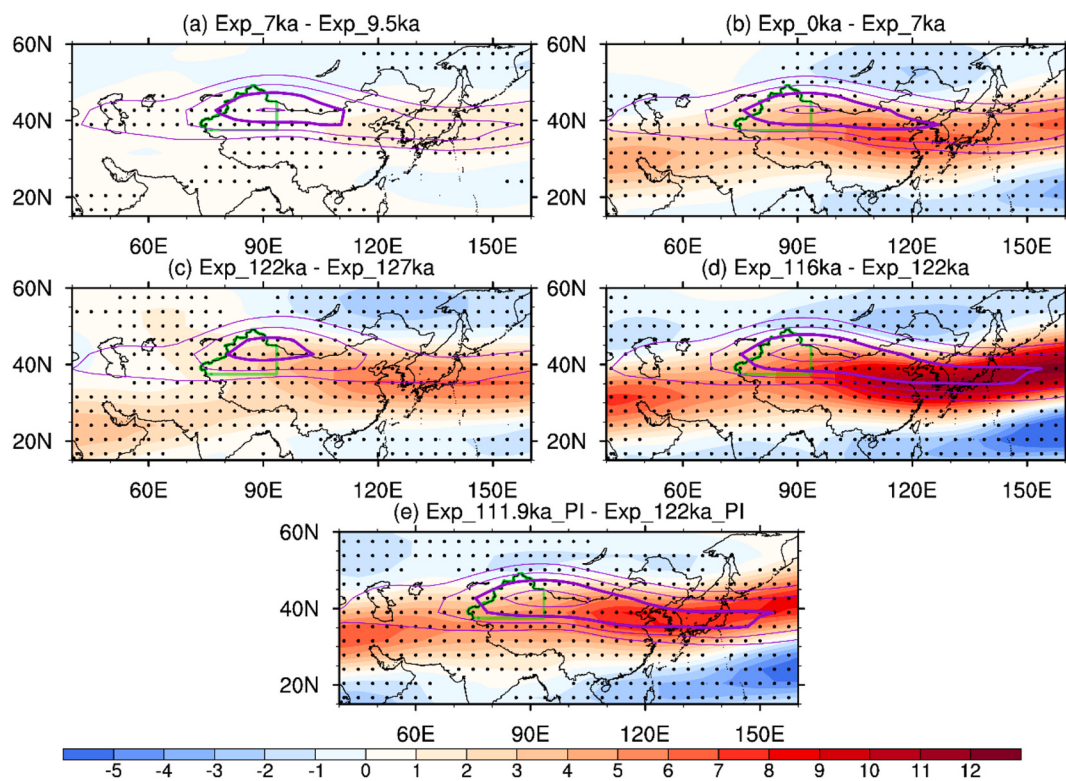


Fig. 6. Composite differences of mean summer half-year zonal wind (m s^{-1} ; shadings) at 200 hPa between Exp_7ka and Exp_9.5ka (a) and between Exp_0ka and Exp_7ka (b) during the Holocene, between Exp_122ka and Exp_127ka (c) and between Exp_116ka and Exp_122ka (d) during the LIG, as well as between Exp_111.9ka_PI and Exp_122ka_PI (e). Dotted regions indicate differences that are significant at the 0.05 confidence level. The contours show the climatological position of the Asian subtropical westerly jet, as indicated by 200 hPa westerly wind maxima (m s^{-1}) at the corresponding longitude in the Exp_9.5ka (a), Exp_7ka (b), Exp_127ka (c), Exp_122ka (d), and Exp_122ka_PI (e). The contour interval is set at 3 m s^{-1} , with the bold contour representing the isoline of 26 m s^{-1} . The study region is outlined by the green contour. (For interpretation of the references to colour in this figure legend, the reader is referred to the web version of this article.)

3.2. Mechanisms of precipitation variations in Northwest China

Precipitation variations in Northwest China are influenced by moisture transport and vertical motions (Shi et al., 2021; Zhang, 2021; Yang et al., 2023). The moisture for precipitation in Northwest China is mainly transported by the mid-latitude westerlies (Jin et al., 2012; Chen et al., 2019). The simulated transport of westerly moisture towards Northwest China was slightly weaker at 7 ka than at 9.5 ka (Fig. 4a). The simulated westerly moisture transport significantly intensified towards the southern region of Northwest China, while it attenuated towards the central and northern regions at 0 ka relative to 7 ka (Fig. 4b). The simulations also reveal a strengthened westerly moisture transport over the southern region of Northwest China, while a weakened westerly moisture transport is simulated over the central and northern regions at 122 ka than at 127 ka and at 116 ka than at 122 ka (Fig. 4c and d). The consistent pattern in anomalous moisture transports was associated with divergent variations in precipitation throughout the LIG (Fig. 3c and d). With the forcing of a lower equatorial spring insolation, anomalous westerly moisture transport (Fig. 4e) and enhanced precipitation (Fig. 3e) were simulated only in the southern region of Northwest China. In general, the moisture transport alone might not sufficiently account for orbital-scale precipitation variations in Northwest China.

As another crucial factor, the simulated mean summer half-year vertical velocity at 500 hPa exhibited no significant changes in Northwest China at 7 ka compared to 9.5 ka (Fig. 5a). This was in line with marginal fluctuations in average summer half-year precipitation during the mid-Holocene relative to the early Holocene (Fig. 3a). Relative to 7 ka, the simulations indicate anomalous upward motions in the southern and central regions of Northwest China, whereas anomalous downward motions were simulated in the northern region at 0 ka (Fig. 5b). The

anomalous upward motions were associated with increased summer half-year precipitation in the southern and central regions of Northwest China, while the anomalous downward motions were associated with weak significant change in summer half-year precipitation in the northern region during the late Holocene relative to the mid-Holocene (Fig. 3b). The wetter condition of Northwest China during the late Holocene can generally be attributed to the anomalous vertical motions. Likewise, precipitation variations simulated in Northwest China during the LIG exhibited a strong correspondence with anomalous vertical motions (Figs. 3 and 5). Therefore, orbital-scale precipitation variations in Northwest China were probably related to atmospheric vertical motions.

The vertical motions exhibit a strong association with the anomalies in upper-level circulation. The dominant circulation of the upper troposphere over Northwest China during the summer half-year is characterized by the presence of the Asian subtropical westerly jet (Schiemann et al., 2009; Chiang et al., 2015). In particular, the core of the Asian subtropical westerly jet is situated over Northwest China during the summer half-year (Zhang et al., 2022b). Compared to 9.5 ka, the zonal wind at 200 hPa was slightly strengthened to the south of the jet axis at 7 ka (Fig. 6a), suggesting a minor southward shift of the Asian subtropical westerly jet (Jiang et al., 2020; Zhang et al., 2024). The strengthening of 200 hPa zonal wind to the south of the jet axis exhibited greater significance between 0 ka and 7 ka than that between 7 ka and 9.5 ka (Fig. 6b). In addition, the zonal wind at 200 hPa was weakened to the north of the jet axis (Fig. 6b). Hence, the Asian subtropical westerly jet experienced a remarkable southward migration at 0 ka compared to 7 ka. Analogously, the southward migration of the Asian subtropical westerly jet between 116 ka and 122 ka was particularly pronounced compared to that between 122 ka and 127 ka (Fig. 6c and d). The Asian

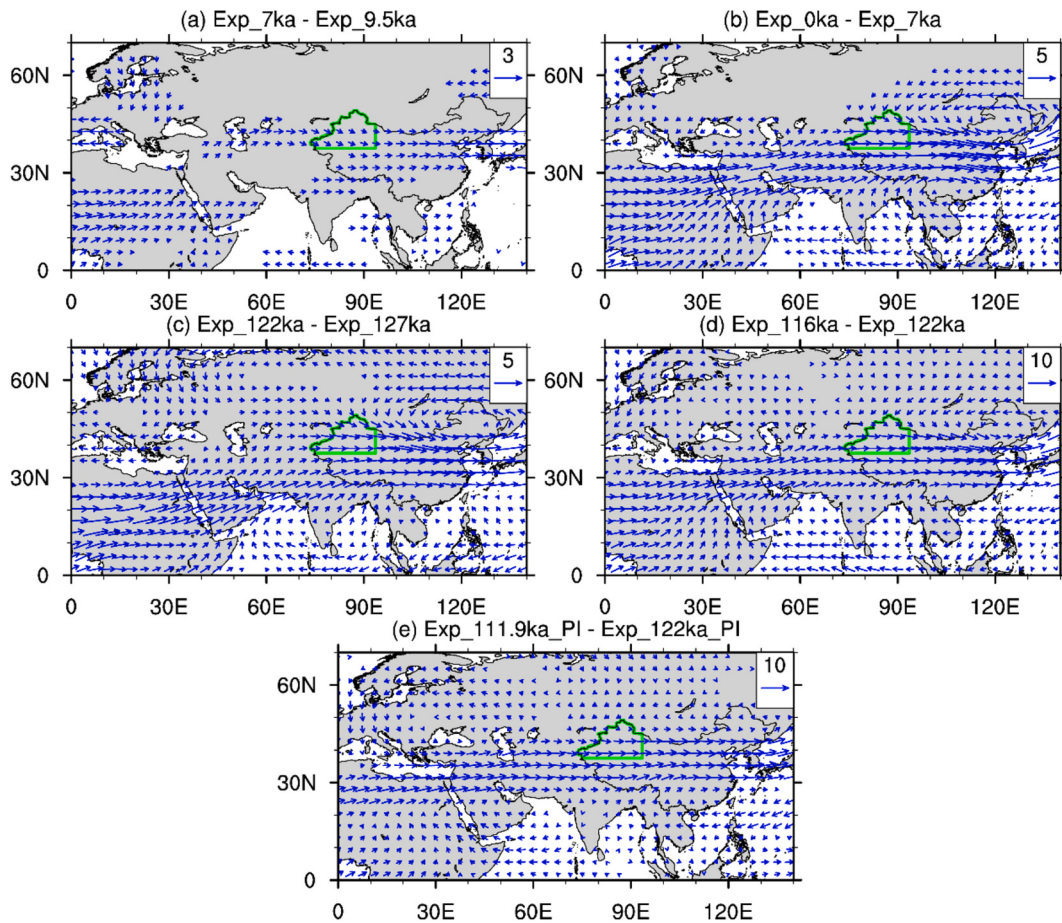


Fig. 7. Composite differences of mean summer half-year winds (m s^{-1}) at 200 hPa between Exp_7ka and Exp_9.5ka (a), between Exp_0ka and Exp_7ka (b) during the Holocene, between Exp_122ka and Exp_127ka (c), between Exp_116ka and Exp_122ka (d) during the LIG, as well as between Exp_111.9ka_PI and Exp_122ka_PI (e). Only differences exceeding the 0.05 significance level are plotted. The study region is outlined by the green contour. (For interpretation of the references to colour in this figure legend, the reader is referred to the web version of this article.)

subtropical westerly jet experienced a slight northward shift in Central Asia at 122 ka compared to 127 ka, as indicated by a greater enhancement of 200 hPa zonal wind in northern Central Asia than that in southern Central Asia (Fig. 6c).

The westerly jet is accompanied by anticyclonic wind shear to the right of its axis (Shapiro, 1982). The upper-level anticyclonic wind shear exhibited no significant change over Northwest China during the summer half-year at 7 ka compared to 9.5 ka (Fig. 7a). In contrast, the simulation results reveal a notable amplification of the anticyclonic wind shear over Northwest China at 0 ka compared to 7 ka (Fig. 7b), in responding to the southward displacement of the Asian subtropical westerly jet (Fig. 6b). Compared to 127 ka, Northwest China was characterized by anomalous cyclonic wind shear in the upper troposphere at 122 ka (Fig. 7c), as a result of enhanced 200 hPa zonal wind over northern Central Asia (Fig. 6c). In contrast, Northwest China exhibited anomalous anticyclonic wind shear in the upper troposphere at 116 ka compared to 122 ka (Fig. 7d), due to the southward migration of the Asian subtropical westerly jet (Fig. 6d).

There was no significant change simulated in the mid-level atmospheric circulation over Northwest China during the summer half-year at 7 ka compared to 9.5 ka (Fig. 8a), which corresponded to a minor shift of the upper-level westerly jet (Figs. 6a and 7a). Relative to 7 ka, anomalous easterlies and westerlies at 600 hPa at 0 ka were simulated over the northern and southern regions of Northwest China, respectively (Fig. 8b). These easterly and westerly anomalies generated anomalous cyclonic wind shear at 600 hPa over Northwest China, which was attributed to the presence of anomalous anticyclone at 200 hPa (Fig. 7b)

due to the baroclinic structure (Jiang et al., 2020). Therefore, there were anomalous upward motions and the resultant increasing precipitation in Northwest China during the late Holocene compared to the mid-Holocene (Figs. 3b and 5b). Compared to 127 ka, Northwest China was dominated by anticyclonic anomalies at 600 hPa at 122 ka as indicated by anomalous westerlies over northern Central Asia and anomalous northwesterlies over the western Mongolia (Fig. 8c). Such anticyclonic anomalies at 600 hPa were associated with anomalous cyclonic wind shear in the upper troposphere over Northwest China (Fig. 7c). Consequently, Northwest China experienced anomalous downward motions and the resultant decreasing precipitation during the mid-LIG compared to the early LIG (Figs. 3c and 5c). Similar to the differences between the late and mid-Holocene, anomalous cyclones at 600 hPa were simulated in Northwest China between the late and mid-LIG (Fig. 8d) in response to upper-level anticyclonic anomalies (Fig. 7d). The related anomalous upward motions (Fig. 5d) resulted in an increase in precipitation over Northwest China during the late LIG compared to the mid-LIG (Fig. 3d). Hence, orbital-scale precipitation variations in Northwest China were influenced by the shift of the Asian subtropical westerly jet, which exerted an impact on vertical motions.

In addition, anomalous cyclonic wind shear at 600 hPa over Northwest China at 0 ka compared to 7 ka, and at 116 ka compared to 122 ka, was associated with significant anticyclonic anomalies extending from the Tibetan Plateau to South China (Fig. 8b and d). The anticyclonic anomalies suppressed the upward motions over the Tibetan Plateau (Fig. 5b and d), resulting from its thermal effects (Wu et al., 2015), which further weakened the compensatory downward motions over

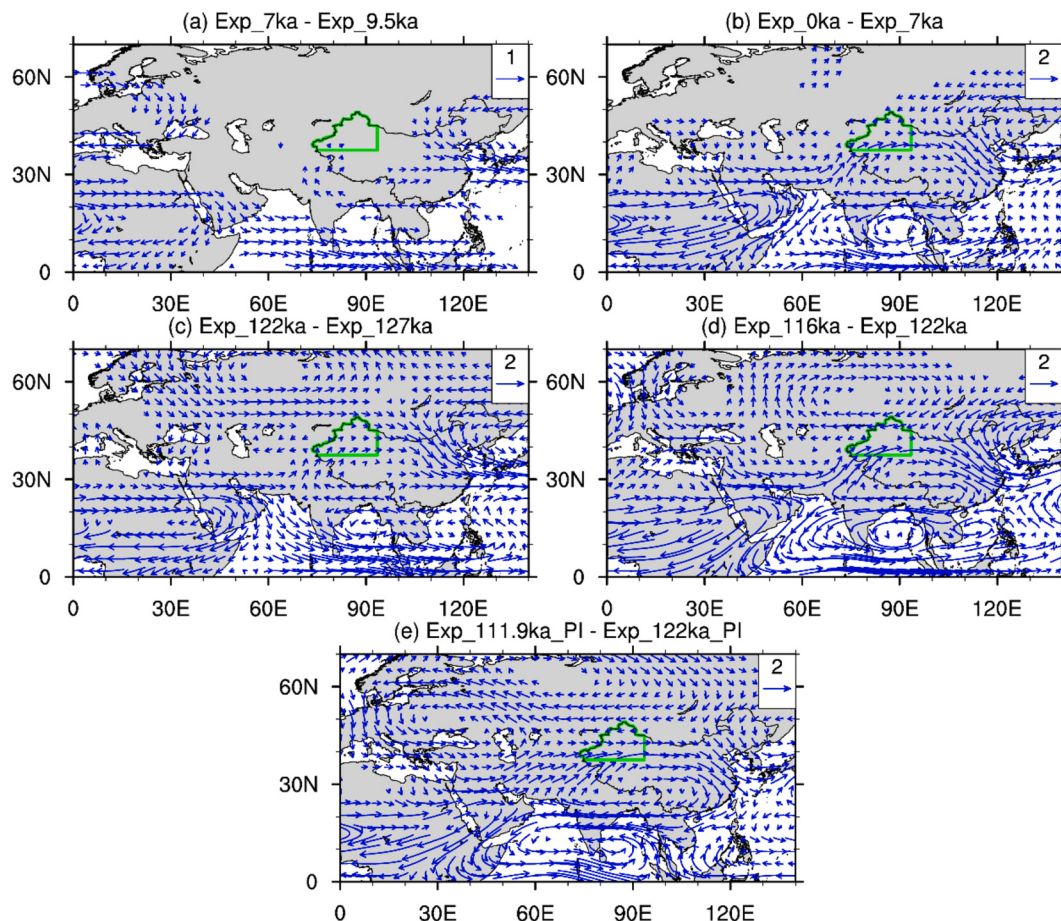


Fig. 8. Composite differences of mean summer half-year winds ($\text{m}\cdot\text{s}^{-1}$) at 600 hPa between Exp_7ka and Exp_9.5ka (a), between Exp_0ka and Exp_7ka (b) during the Holocene, between Exp_122ka and Exp_127ka (c), between Exp_116ka and Exp_122ka (d) during the LIG, as well as between Exp_111.9ka_PI and Exp_122ka_PI (e). Only differences exceeding the 0.05 significance level are plotted. The study region is outlined by the green contour. (For interpretation of the references to colour in this figure legend, the reader is referred to the web version of this article.)

Northwest China. Consequently, Northwest China exhibited anomalous upward motions (Fig. 5b and d) and enhanced precipitation (Fig. 3b and d) at 0 ka compared to 7 ka, and at 116 ka compared to 122 ka.

The anticyclonic anomalies over South China are closely related to the western Pacific subtropical high (WPSH) in the mid-troposphere during the summer half-year (Zhou et al., 2009). The WPSH exhibited a significant enhancement and westward extension at 0 ka compared to 7 ka, and at 116 ka compared to 122 ka, as evidenced by increased geopotential height at 500 hPa over South China (Fig. 9b and d). The westward extension of the WPSH contributed to the development of anticyclonic anomalies over South China, which subsequently reinforced the anticyclonic anomalies over the Tibetan Plateau (Fig. 8b and d). The enhancement and westward extension of the WPSH were not obvious at 7 ka compared to 9.5 ka, and at 122 ka compared to 127 ka (Fig. 9a and c). Accordingly, the anomalous subsidence over the Tibetan Plateau was less pronounced (Fig. 5a and c). Hence, orbital-scale precipitation variations in Northwest China were also influenced by the shift of the WPSH.

3.3. Mechanisms of orbital forcing

The enhancement of the Asian subtropical westerly jet was associated with anomalous upper-level anticyclone over South Asia, specifically an enhanced South Asian High (SAH) (Fig. 7). In the tropics, upper-level anticyclonic anomalies are significantly influenced by the surface heating through the Matsuno–Gill response (Gill, 1980; Matsuno, 1966). The surface heating induces anomalous upper-level

anticyclone to the northwest of the heat source (Gill, 1980). Hence, anomalous upper-level anticyclone over South Asia might be significantly affected by SST anomalies over the IPWP. The WPSH is the subside branch of the Hadley Cell (Song et al., 2018). SST anomalies over the IPWP exert a significant influence on the ascending branch of the Hadley Cell, which may subsequently affect the WPSH.

The IPWP exhibited a cooling during the summer half-year at 7 ka compared to 9.5 ka (Fig. 10a) and a significant warming at 0 ka than at 7 ka (Fig. 10b). Similarly, a significant cooling was simulated over the tropical Indian Ocean at 122 ka compared to 127 ka (Fig. 10c). Meanwhile, an overall warming was simulated over the IPWP at 116 ka relative to 122 ka (Fig. 10d). According to the Matsuno–Gill mechanism (Gill, 1980; Matsuno, 1966), the IPWP cooling favored the formation of anomalous upper-level cyclone over South Asia at 7 ka and 122 ka compared to 9.5 ka and 127 ka, respectively (Fig. 11a, c). In contrast, the IPWP warming facilitated the development of anomalous upper-level anticyclone over South Asia at 0 ka and 116 ka relative to 7 ka and 122 ka, respectively (Fig. 11b, d). The anomalous upper-level cyclone over South Asia weakened the enhancement of the Asian subtropical westerly jet, which was initially strengthened by summer insolation forcing (Wang et al., 2020; Yang et al., 2023; Zhang et al., 2024). On the contrary, the enhancement of the Asian subtropical westerly jet was strengthened by the anomalous upper-level anticyclone. Therefore, the Asian subtropical westerly jet experienced a more notable enhancement and southward shift between 0 ka and 7 ka (Fig. 7b), and between 116 ka and 122 ka (Fig. 7d).

It is obvious that spring insolation exerted a positive effect on

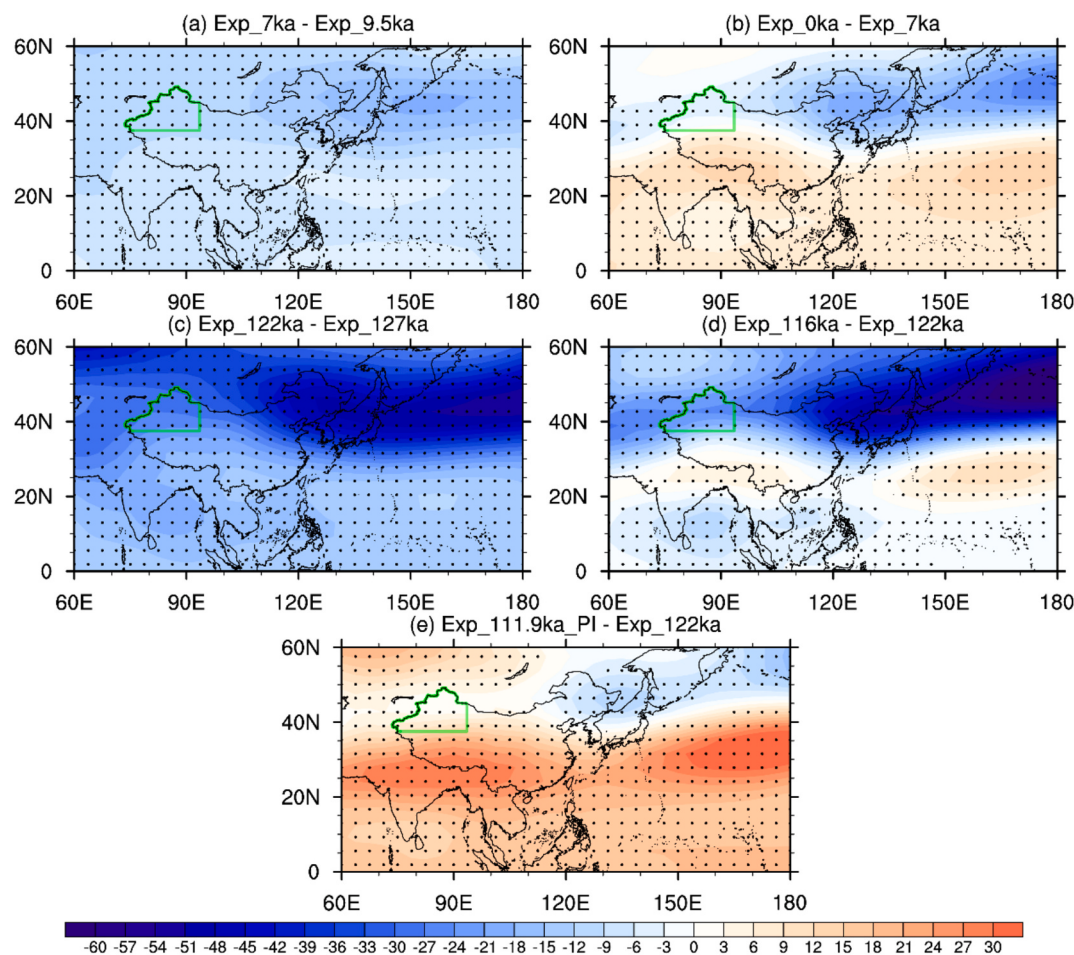


Fig. 9. Composite differences of mean summer half-year eddy geopotential height (gpm) at 500 hPa between Exp_7ka and Exp_9.5ka (a) and between Exp_0ka and Exp_7ka (b) during the Holocene, between Exp_122ka and Exp_127ka (c) and between Exp_116ka and Exp_122ka (d) during the LIG, as well as between Exp_111.9ka_PI and Exp_122ka_PI (e). Dotted regions indicate differences that are significant at the 0.05 confidence level. The study region is outlined by the green contour. (For interpretation of the references to colour in this figure legend, the reader is referred to the web version of this article.)

variations of the IPWP SST as shown by the difference between simulations with distinct levels of spring insolation (between Exp_122ka_PI and Exp_111.9ka_PI) (Fig. 10e). The IPWP warming between 0 ka and 7 ka (Fig. 10b) and between 116 ka and 122 ka BP (Fig. 10d) was consistent with the increased spring insolation but contrasted sharply with the decreased summer insolation (Fig. 1a). The association between the IPWP SST and spring insolation during the Holocene is also supported by records from Cores SO188–17286-1 (Wang et al., 2022), RC12-344 (Rashid et al., 2007), and SO139-74KL (Lückge et al., 2009) (Fig. 12). This suggests that the effect of spring insolation on variations of the IPWP SST in the summer half-year overwhelmed that of summer insolation. This is possible because that the IPWP received a maximum insolation during the spring season (Berger and Loutre, 1991). Hence, the IPWP SST in the summer half-year was significantly influenced by spring insolation at the equator.

The IPWP warming (Fig. 10e) induced anomalous upper-level anticyclone over South Asia, and the resultant enhancement and southward shift of the SAH with a higher spring insolation at the equator (Fig. 11e). Consequently, anomalous cyclone at 600 hPa over the Northwest China (Fig. 8e) was induced by the enhancement and southward displacement of the Asian subtropical westerly jet (Figs. 6e and 7e). The cyclonic anomalies generated anomalous upward motions (Fig. 5e) and ultimately increased precipitation in Northwest China (Fig. 3e).

In addition, the IPWP warming strengthened the Hadley Circulation, leading to an enhancement of the WPSH (Fig. 9e). The enhancement of the WPSH contributed to the formation of mid-tropospheric anticyclonic

anomalies over the Tibetan Plateau (Fig. 8e). These anticyclonic anomalies suppressed the upward motions over the Tibetan Plateau and weakened the compensatory downward motions over Northwest China (Wu et al., 2015). Accordingly, there were anomalous upward motions (Fig. 5e) and ultimately increased precipitation in Northwest China (Fig. 3e). Therefore, the wetter conditions during the late periods of the Holocene and LIG likely originated from an increased spring insolation at the equator. The equatorial spring insolation played an important role in modulating orbital-scale precipitation variations in Northwest China.

4. Summary and discussions

Proxy records indicate that Northwest China generally experienced negligible moisture changes or a drying trend during the early to mid-Holocene, followed by a subsequent wetting trend (Chen et al., 2016; Xu et al., 2019; Lan et al., 2021). The moisture pattern in Northwest China exhibited an inverse relationship with those recorded in regions dominated by the ASM at orbital timescale during the Holocene (Chen et al., 2019, 2022; Xu et al., 2019; Lan et al., 2021; Zhang, 2021). This evolution pattern has been proposed to be influenced by factors, such as ice sheet (Lan et al., 2021), orbital forcing (Chen et al., 2016; Lan et al., 2021; Wang et al., 2022b; Zhang et al., 2022c), tropical Indian Ocean SST (Yang et al., 2023), and evaporation (Rao et al., 2019; Xu et al., 2019). However, the underlying physical mechanisms remain incompletely elucidated.

In this study, we conducted a comparative analysis of summer half-

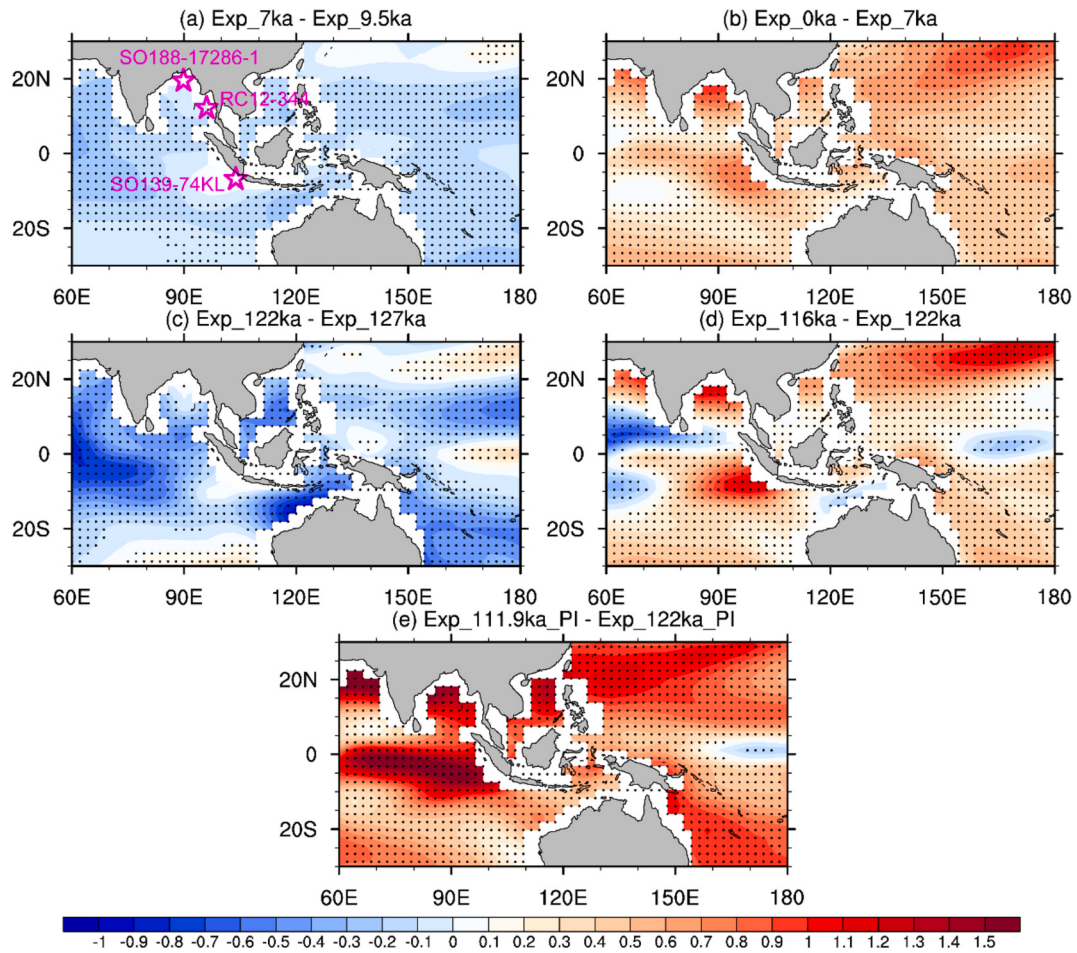


Fig. 10. Composite differences of mean summer half-year SST ($^{\circ}\text{C}$) between Exp_7ka and Exp_9.5ka (a), between Exp_0ka and Exp_7ka (b) during the Holocene, between Exp_122ka and Exp_127ka (c), between Exp_116ka and Exp_122ka (d) during the LIG, as well as between Exp_111.9ka_PI and Exp_122ka_PI (e). Dotted regions indicate differences that are significant at the 0.05 confidence level.

year precipitation variations in Northwest China during the Holocene and LIG (an analog for the Holocene; [Bova et al., 2021](#)) based on climate simulations by the CESM, aiming to enhance our understanding of the underlying physical mechanisms. These simulations are mainly forced by Earth's orbital parameters and concentrations of greenhouse gases. We neglect the forcing of ice sheets in our simulations. Our simulations demonstrate a minor precipitation change between the mid- and early Holocene, and a significant increase in precipitation between the late and mid-Holocene. The simulation results demonstrate a strong agreement with proxy records regarding the Holocene precipitation changes in Northwest China (e.g., [Liu et al., 2008](#); [Wang et al., 2013](#); [Hong et al., 2014](#); [Chen et al., 2016](#); [Liu et al., 2020](#); [Jia et al., 2021](#)). Furthermore, the simulations show a substantial decline in precipitation across Northwest China between the mid- and early LIG, and a notable increase between the late and mid-LIG. These simulation results have not been validated by proxy records due to the substantial uncertainties in chronologies during the LIG. The Holocene and LIG simulations reveal that orbital-scale precipitation variations in Northwest China generally corresponded to spring insolation at the equator. The summer half-year precipitation in Northwest China exhibited a significant increase in response to reduced spring insolation at the equator, as evidenced by further simulations. Therefore, it is likely that the orbital-scale precipitation patterns in Northwest China were influenced by spring insolation at the equator.

Orbital-scale precipitation variations in Northwest China were closely related to the meridional displacement of the Asian subtropical westerly jet and the zonal shift of the WPSH. The intensified westerlies at

200 hPa, located south of the jet axis, resulted in a southward displacement of the Asian subtropical westerly jet during the late periods of the Holocene and LIG. The southward displacement of the Asian subtropical westerly jet was associated with upper-level anticyclonic anomalies over Northwest China, leading to anomalous upward motions in the lower and mid-troposphere. The westward extension of the WPSH further enhanced these anomalous upward motions via suppressing the upward motions over the Tibetan Plateau. Consequently, precipitation enhanced in Northwest China as a result of the southward displacement of the Asian subtropical westerly jet and the westward extension of the WPSH. Many previous studies also attributed the increase of precipitation over Northwest China to the southward migration of the Asian subtropical westerly jet during the Holocene ([Lan et al., 2021](#); [Wang et al., 2022b](#); [Zhang et al., 2022c](#)). The key mechanism involved was the intensified westerly moisture transport towards Northwest China resulting from the southward migration of the Asian subtropical westerly jet ([Lan et al., 2021](#); [Wang et al., 2022b](#); [Zhang et al., 2022c](#)). Our simulations did not exhibit significant enhancement of westerly moisture transport with the southward migration of the Asian subtropical westerly jet ([Fig. 4](#)). The southward migration of the Asian subtropical westerly jet was only associated with enhanced southward moisture transport towards the southern region of Northwest China. We focused on the role of anomalous upward motions in attributing the increase in precipitation in Northwest China to the southward migration of the Asian subtropical westerly jet, as also emphasized by [Jiang et al. \(2020\)](#) and [Shi et al. \(2021\)](#).

The strength of the Asian subtropical westerly jet is mainly

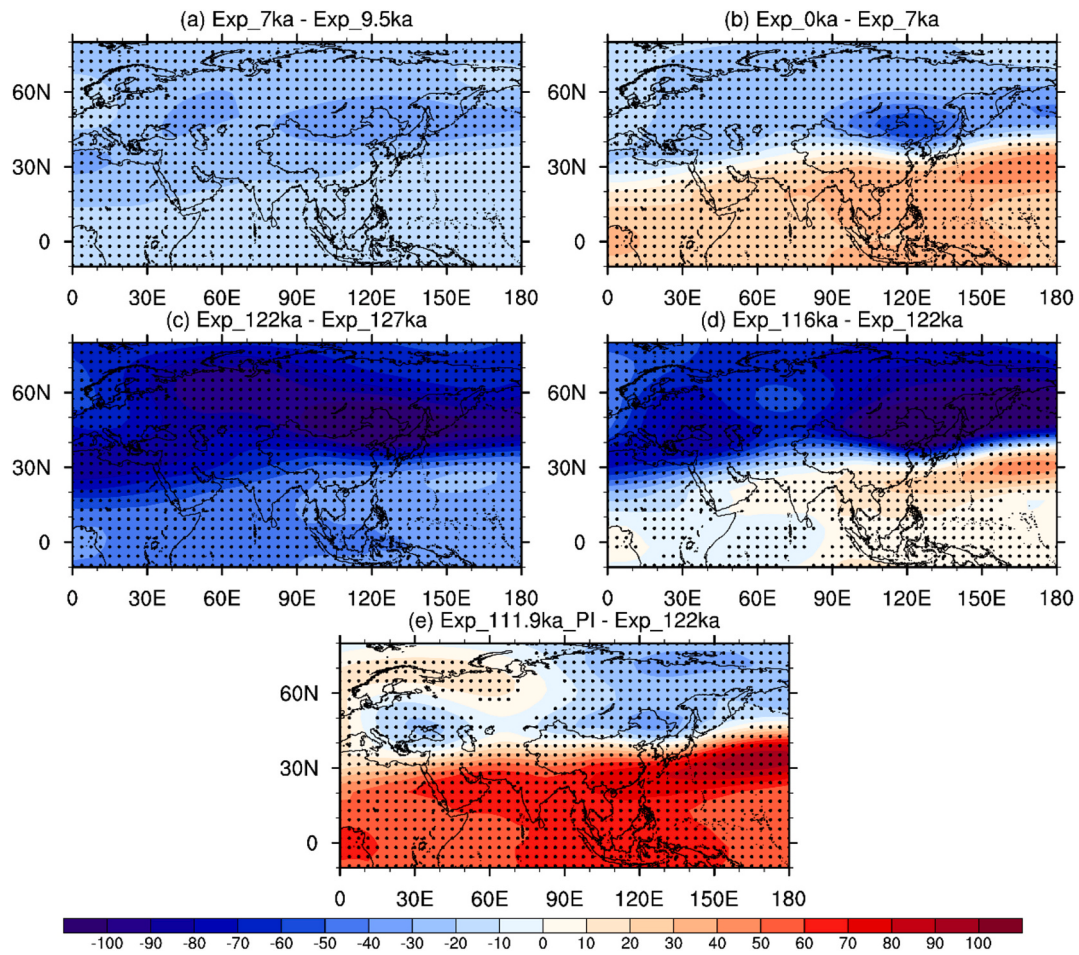


Fig. 11. Composite differences of mean summer half-year geopotential height (gpm) at 200 hPa between Exp_7ka and Exp_9.5ka (a), between Exp_0ka and Exp_7ka (b) during the Holocene, between Exp_122ka and Exp_127ka (c), between Exp_116ka and Exp_122ka (d) during the LIG, as well as between Exp_111.9ka_PI and Exp_122ka_PI (e). Dotted regions indicate differences that are significant at the 0.05 confidence level.

controlled by the meridional thermal gradient from the tropical Indian Ocean to northern Eurasia, which is dominated by summer insolation forcing (Wang et al., 2020; Yang et al., 2023; Zhang et al., 2024). In addition, the Asian subtropical westerly jet was significantly enhanced by anomalous anticyclone over South Asia. The interplay between the Asian subtropical westerly jet and the South Asian upper-level anticyclone (i.e., the SAH) is schematically illustrated in Fig. 13. The anomalous anticyclone was induced through the Matsuno–Gill response (Gill, 1980; Jiang et al., 2020; Matsuno, 1966), which was triggered by the warming of the IPWP.

Our simulated changes in IPWP SST during the summer half-year (April–September) show a strong alignment with some records for the Holocene. However, these changes exhibit significant discrepancies compared to SST changes documented in numerous other IPWP records, which are closely associated with variations in winter or summer insolation (Bova et al., 2021; Leduc et al., 2010). The discrepancies observed between different records, as well as between records and simulations, are likely attributable to seasonal biases inherent in SST reconstructions (Kaufman and Broadman, 2023; Liu et al., 2014).

In addition, it should be noted that our simulations indicate a significant increase in 200 hPa westerlies over northern Central Asia and the resultant northward shift of the Asian subtropical westerly jet over Central Asia during the mid-LIG compared to the early LIG (Fig. 6c). This northward shift of the Asian subtropical westerly jet over Central Asia was the key for the decrease of precipitation in Northwest China between the mid- and early LIG. The increase of 200 hPa westerlies over northern Central Asia was mainly related to anomalous cyclone over

Central Russia (Fig. 7c). The anomalous cyclone over Central Russia was also associated with reduced equatorial spring insolation (Exp_122ka_PI – Exp_111.9ka_PI; Fig. 7e). This might be related to the tropical Indian Ocean cooling, which was also controlled by equatorial spring insolation (Zhang et al., 2024). According to Huang et al. (2015a, 2015b), the tropical Indian Ocean warming motivates a meridional teleconnection, with anomalous cyclone over Central Asia sandwiched by anomalous anticyclones over the tropical Indian Ocean and Central Russia. This meridional teleconnection is also evident in our simulations (Fig. 7e). In contrast, the tropical Indian Ocean cooling resulting from reduced equatorial spring insolation likely triggered anomalous cyclone over Central Russia. Accordingly, the westerly jet enhanced over northern Central Asia during the mid-LIG compared to the early LIG in response to the decrease in equatorial spring insolation. Ultimately, precipitation decreased over Northwest China during the mid-LIG compared to the early LIG.

In conclusion, orbital-scale precipitation variability over Northwest China was significantly influenced by changes in equatorial spring insolation. The associated mechanisms are summarized in Fig. 14. The summer half-year precipitation in Northwest China exhibited a notable enhancement, accompanied by an increase in equatorial spring insolation. Between the mid- and early Holocene, the marginal decrease in equatorial spring insolation did not result in a significant reduction in precipitation levels in Northwest China. Between the late and mid-Holocene, the pronounced increase in equatorial spring insolation led to a substantial augmentation of precipitation in Northwest China. Consequently, a discernible increase in precipitation has been recorded

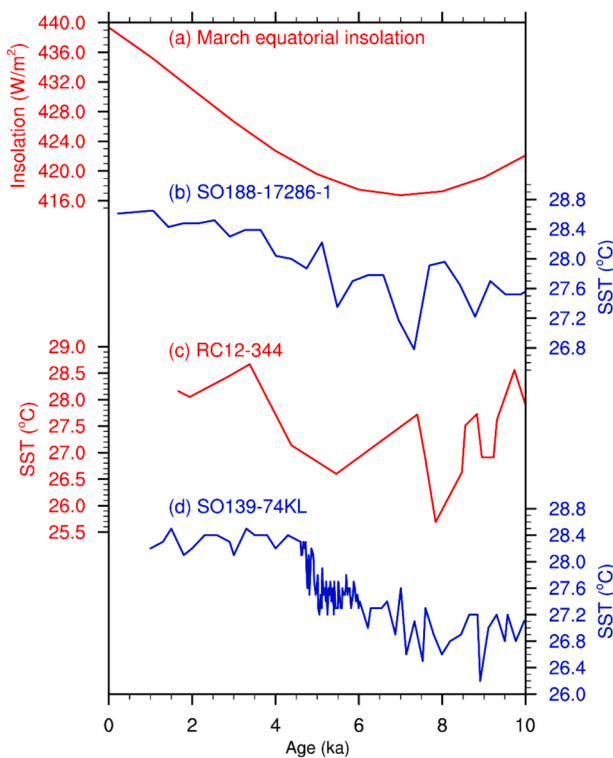


Fig. 12. Holocene evolution of March insolation at 0° (Laskar et al., 2004) (a) and SSTs over the IPWP recorded in Cores SO188-17286-1 (Wang et al., 2022) (b), RC12-344 (Rashid et al., 2007) (c), and SO139-74KL (Lückge et al., 2009) (d). The locations of these records are shown in Fig. 10a and Table 2.

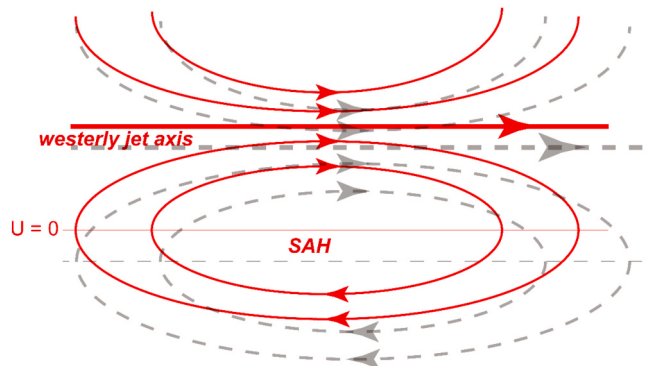


Fig. 13. Schematic diagram showing the interplay between the Asian subtropical westerly jet and SAH. The Asian subtropical westerly jet is accompanied by an anticyclone to the right of its axis, specifically the SAH over the Tibetan Plateau. The ridge of the SAH is characterized by maximum geopotential height and zero zonal wind. The enhancement and southward displacement of the SAH are associated with anomalous westerlies south of the westerly jet axis and the resulting southward shift of the Asian subtropical westerly jet (indicated by the transition from red to gray streamlines). (For interpretation of the references to colour in this figure legend, the reader is referred to the web version of this article.)

and simulated in Northwest China since the mid-Holocene, which can be attributed to the concurrent rise in equatorial spring insolation. Precession induced much greater changes in seasonal insolation during the LIG than that during the Holocene (Berger and Loutre, 1991; Bova et al., 2021). Equatorial spring insolation exhibited a significant decreasing trend from the early to mid-LIG, and a notable increasing trend from the mid- to late Holocene. Accordingly, there was a drying in Northwest China between the mid- and early LIG, and a wetting between the late

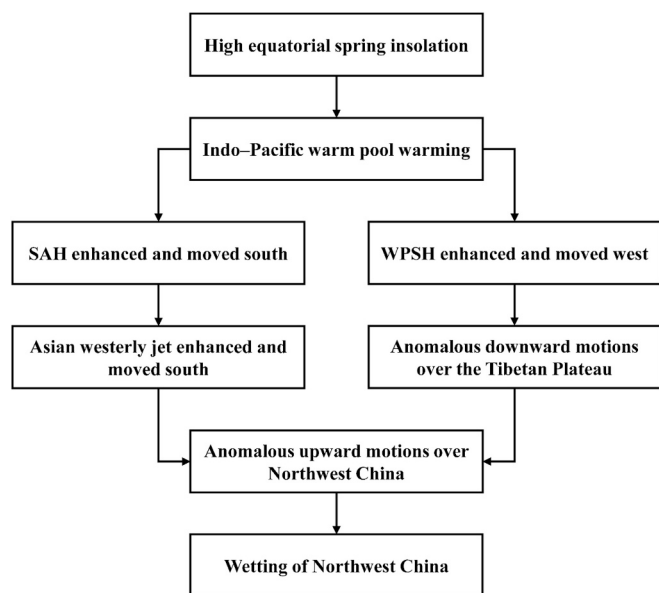


Fig. 14. Illustration showing the mechanisms for the influence of equatorial spring insolation on orbital-scale precipitation variation in Northwest China.

and mid-LIG. Ultimately, orbital-scale precipitation variability in Northwest China exhibited a close, yet none-linear response to the precession.

CRediT authorship contribution statement

Yunxia Gan: Writing – original draft, Visualization, Investigation, Formal analysis. **Ziyu Zhou:** Writing – review & editing, Visualization, Validation, Formal analysis. **Xiaojian Zhang:** Writing – review & editing, Writing – original draft, Visualization, Supervision, Software, Methodology, Investigation, Formal analysis, Data curation, Conceptualization.

Declaration of competing interest

The authors declare that they have no known competing financial interests or personal relationships that could have appeared to influence the work reported in this paper.

Acknowledgements

The numerical simulations in this paper have been done in the High Performance Computing Center (HPCC) of Nanjing University. We acknowledge the support provided by the National Key Research and Development Program of China (Grant No. 2023YFF0804703), the National Natural Science Foundation of China (Grant No. 42171152), and the ‘GeoX’ Interdisciplinary Project of Frontiers Science Center for Critical Earth Material Cycling (Grant No. 20250204).

Appendix A. Supplementary data

Supplementary data to this article can be found online at <https://doi.org/10.1016/j.palaeo.2025.113184>.

Data availability

Data will be made available on request.

References

- Berger, A., Loutre, M.F., 1991. Insolation values for the climate of the last 10 million years. *Quat. Sci. Rev.* 10, 297–317. [https://doi.org/10.1016/0277-3791\(91\)90033-Q](https://doi.org/10.1016/0277-3791(91)90033-Q).
- Bova, S., Rosenthal, Y., Liu, Z., Godad, S.P., Yan, M., 2021. Seasonal origin of the thermal maxima at the Holocene and the last interglacial. *Nature* 589, 548–553. <https://doi.org/10.1038/s41586-020-03155-x>.
- Cai, Y., Chiang, J.C.H., Breitenbach, S.F.M., Tan, L., Cheng, H., Edwards, R.L., An, Z., 2017. Holocene moisture changes in western China, Central Asia, inferred from stalagmites. *Quat. Sci. Rev.* 158, 15–28. <https://doi.org/10.1016/j.quascirev.2016.12.014>.
- Chen, F., Jia, J., Chen, J., Li, G., Zhang, X., Xie, H., Xia, D., Huang, W., An, C., 2016. A persistent Holocene wetting trend in arid Central Asia, with wettest conditions in the late Holocene, revealed by multi-proxy analyses of loess-paleosol sequences in Xinjiang, China. *Quat. Sci. Rev.* 146, 134–146. <https://doi.org/10.1016/j.quascirev.2016.06.002>.
- Chen, F., Chen, J., Huang, W., Chen, S., Huang, X., Jin, L., Jia, J., Zhang, X., An, C., Zhang, J., Zhao, Y., Yu, Z., Zhang, R., Liu, J., Zhou, A., Feng, S., 2019. Westerlies Asia and monsoonal Asia: spatiotemporal differences in climate change and possible mechanisms on decadal to sub-orbital timescales. *Earth Sci. Rev.* 192, 337–354. <https://doi.org/10.1016/j.earscirev.2019.03.005>.
- Chen, C., Zhang, X., Lu, H., Jin, L., Du, Y., Chen, F., 2021. Increasing summer precipitation in arid Central Asia linked to the weakening of the East Asian summer monsoon in the recent decades. *Int. J. Climatol.* 41, 1024–1038. <https://doi.org/10.1002/joc.6727>.
- Chen, S., Chen, J., Lv, F., Liu, X., Huang, W., Wang, T., Liu, J., Hou, J., Chen, F., 2022. Holocene moisture variations in arid Central Asia: reassessment and reconciliation. *Quat. Sci. Rev.* 297, 107821. <https://doi.org/10.1016/j.quascirev.2022.107821>.
- Cheng, H., Zhang, P., Spötl, C., Edwards, R.L., Cai, Y., Zhang, D., Sang, W., Tan, M., An, Z., 2012. The climatic cyclicity in semiarid-arid Central Asia over the past 500,000 years. *Geophys. Res. Lett.* 39, 2011GL050202. <https://doi.org/10.1029/2011GL050202>.
- Chiang, J.C.H., Fung, I.Y., Wu, C.H., Cai, Y., Labrousse, C.A., 2015. Role of seasonal transitions and westerly jets in East Asian paleoclimate. *Quat. Sci. Rev.* 108, 111–129. <https://doi.org/10.1016/j.quascirev.2014.11.009>.
- Craig, A.P., Vertenstein, M., Jacob, R., 2012. A new flexible coupler for earth system modeling developed for CCSM4 and CESM1. *Int. J. High Perform. Comput. Appl.* 26, 31–42. <https://doi.org/10.1177/1094342011428141>.
- Danabasoglu, G., Bates, S.C., Briegleb, B.P., Jayne, S.R., Jochum, M., Large, W.G., Peacock, S., Yeager, S.G., 2012. The CCSM4 ocean compo. *J. Clim.* 25, 1361–1389. <https://doi.org/10.1175/JCLI-D-11-00091.1>.
- Davis, B.A., Brewer, S., 2009. Orbital forcing and role of the latitudinal insolation/temperature gradient. *Clim. Dyn.* 32, 143–165. <https://doi.org/10.1007/s00382-008-0480-9>.
- Ding, Y., Wu, P., Liu, Y., 2022. Modulation of sea surface temperature in three oceans on precipitation increase over Northwest China during the past 60 years: a review. *Front. Clim.* 4, 1015225. <https://doi.org/10.3389/fclim.2022.1015225>.
- Galbraith, R.F., Roberts, R.G., 2012. Statistical aspects of equivalent dose and error calculation and display in OSL dating: an overview and some recommendations. *Quat. Geochronol.* 11, 1–27. <https://doi.org/10.1016/j.quageo.2012.04.020>.
- Gill, A.E., 1980. Some simple solutions for heat-induced tropical circulation. *Q. J. R. Meteorol. Soc.* 106 (449), 447–462. <https://doi.org/10.1002/qj.49710644905>.
- Hong, B., Gasse, F., Uchida, M., Hong, Y., Leng, X., Shibata, Y., Wang, Y., 2014. Increasing summer rainfall in arid eastern-Central Asia over the past 8500 years. *Sci. Rep.* 4, 5279. <https://doi.org/10.1038/srep05279>.
- Huang, W., Chen, J., Zhang, X., Feng, S., Chen, F., 2015a. Definition of the core zone of the ‘westerlies-dominated climatic regime’, and its controlling factors during the instrumental period. *Sci. China Earth Sci.* 58 (5), 676–684. <https://doi.org/10.1007/s11430-015-5057-y>.
- Huang, W., Feng, S., Chen, J., Chen, F., 2015b. Physical mechanisms of summer precipitation variations in the tarim basin in northwestern China. *J. Clim.* 28, 3579–3591. <https://doi.org/10.1175/JCLI-D-14-00395.1>.
- Hunke, E.C., Lipscomb, W.H., 2008. CICE: The Los Alamos Sea Ice Model, Documentation and Software User’s Manual, Version 4.0 (Tech. Rep. LA-CC-06-012). Los Alamos National Laboratory, Los Alamos, NM.
- Hurrell, J.W., Holland, M.M., Gent, P.R., Ghosh, S., Kay, J.E., Kushner, P.J., Lamarque, J.F., Large, W.G., Lawrence, D., Lindsay, K., Lipscomb, W.H., Long, M.C., Mahowald, N., Marsh, D.R., Neale, R.B., Rasch, P., Vavrus, S., Vertenstein, M., Bader, D., Collins, W.D., Hack, J.J., Kiehl, J., Marshall, S., 2013. The community earth system model: a framework for collaborative research. *Bull. Am. Meteorol. Soc.* 94, 1339–1360. <https://doi.org/10.1175/BAMS-D-12-00121.1>.
- Jia, J., Chen, J., Wang, Z., Chen, S., Wang, Q., Wang, L., Yang, L., Xia, D., Chen, F., 2021. No evidence for an anti-phased Holocene moisture regime in mountains and basins in Central Asian records from Ili loess, Xinjiang. *Palaeogeogr. Palaeoclimatol. Palaeoecol.* 572, 110407. <https://doi.org/10.1016/j.palaeo.2021.110407>.
- Jiang, D., Lang, X., Tian, Z., Ju, L., 2013. Mid-holocene East Asian summer monsoon strengthening: insights from paleoclimate modeling intercomparison project (PMIP) simulations. *Palaeogeogr. Palaeoclimatol. Palaeoecol.* 369, 422–429. <https://doi.org/10.1016/j.palaeo.2012.11.007>.
- Jiang, N., Yan, Q., Xu, Z., Shi, J., Zhang, R., 2020. The meridional shift of the midlatitude westerlies over Arid Central Asia during the past 21 000 years based on the TraCE-21ka simulations. *J. Clim.* 33, 7455–7478. <https://doi.org/10.1175/JCLID-19-0798.1>.
- Jin, L., Chen, F., Morrill, C., Otto-Bliesner, B.L., Rosenbloom, N., 2012. Causes of early Holocene desertification in arid Central Asia. *Clim. Dyn.* 38, 1577–1591. <https://doi.org/10.1007/s00382-011-1086-1>.
- Kaufman, D.S., Broadman, E., 2023. Revisiting the Holocene global temperature conundrum. *Nature* 614, 425–435. <https://doi.org/10.1038/s41586-022-05536-w>.
- Lan, J., Wang, T., Dong, J., Kang, S., Cheng, P., Zhou, K., Liu, X., Wang, Y., Ma, L., 2021. The influence of ice sheet and solar insolation on holocene moisture evolution in northern central asia. *Earth Sci. Rev.* 217, 103645. <https://doi.org/10.1016/j.earscirev.2021.103645>.
- Laskar, J., Robutel, P., Joutel, F., Gastineau, M., Correia, A.C.M., Levrard, B., 2004. A long-term numerical solution for the insolation quantities of the Earth. *Astron. Astrophys.* 428, 261–285. <https://doi.org/10.1051/0004-6361:20041335>.
- Lawrence, D.M., Oleson, K.W., Flanner, M.G., Thornton, P.E., Swenson, S.C., Lawrence, P.J., Zeng, X., Yang, Z.L., Levis, S., Sakaguchi, K., Bonan, G.B., Slater, A.G., 2011. Parameterization improvements and functional and structural advances in version 4 of the community land model. *J. Adv. Model. Earth Syst.* 3, M03001. <https://doi.org/10.1029/2011MS00045>.
- Leduc, G., Schneider, R., Kim, J.-H., Lohmann, G., 2010. Holocene and Eemian sea surface temperature trends as revealed by alkenone and Mg/Ca paleothermometry. *Quat. Sci. Rev.* 29, 989–1004. <https://doi.org/10.1016/j.quascirev.2010.01.004>.
- Li, G., Yang, H., Stevens, T., Zhang, X., Zhang, H., Wei, H., Zheng, W., Li, L., Liu, X., Chen, J., Xia, D., Oldknow, C., Ye, W., Chen, F., 2020. Differential ice volume and orbital modulation of Quaternary moisture patterns between Central and East Asia. *Earth Planet. Sci. Lett.* 530, 115901. <https://doi.org/10.1016/j.epsl.2019.115901>.
- Liu, X., Herzschuh, U., Shen, J., Jiang, Q., Xiao, X., 2008. Holocene environmental and climatic changes inferred from Wulung Lake in northern Xinjiang, China. *Quat. Res.* 70, 412–425. <https://doi.org/10.1016/j.yqres.2008.06.005>.
- Liu, Z., Zhu, J., Rosenthal, Y., Zhang, X., Otto-Bliesner, B.L., Timmermann, A., Smith, R.S., Lohmann, G., Zheng, W., Timm, O.E., 2014. The Holocene temperature conundrum. *Proc. Natl. Acad. Sci. USA* 111, E3501–E3505. <https://doi.org/10.1073/pnas.1407229111>.
- Liu, X., Liu, J., Shen, C., Yang, Y., Chen, J., Chen, S., Wang, X., Wu, C., Chen, F., 2020. Inconsistency between records of $\delta^{18}\text{O}$ and trace element ratios from stalagmites: evidence for increasing mid-late Holocene moisture in arid Central Asia. *Holocene* 30, 369–379. <https://doi.org/10.1177/0959683619887431>.
- Loulorgue, L., Schilt, A., Spahni, R., Masson-Delmotte, V., Blunier, T., Lemieux, B., Barnola, J.-M., Raynaud, D., Stocker, T.F., Chappellaz, J., 2008. Orbital and millennial-scale features of atmospheric CH_4 over the past 800,000 years. *Nature* 453, 383–386. <https://doi.org/10.1038/nature06950>.
- Lückge, A., Mohtadi, M., Rühlemann, C., Scheeder, G., Vink, A., Reinhardt, L., Wiedicke, M., 2009. Monsoon versus ocean circulation controls on paleoenvironmental conditions off southern Sumatra during the past 300,000 years. *Paleoceanography* 24, PA1208. <https://doi.org/10.1029/2008PA001627>.
- Lüthi, D., Le Floch, M., Bereiter, B., Blunier, T., Barnola, J.-M., Siegenthaler, U., Raynaud, D., Jouzel, J., Fischer, H., Kawamura, K., Stocker, T.F., 2008. High-resolution carbon dioxide concentration record 650,000–800,000 years before present. *Nature* 453, 379–382. <https://doi.org/10.1038/nature06949>.
- Marcott, S.A., Shakun, J.D., Clark, P.U., Mix, A.C., 2013. A reconstruction of regional and global temperature for the past 11,300 years. *Science* 339, 1198–1201. <https://doi.org/10.1126/science.1228026>.
- Matsuno, T., 1966. Quasi-geostrophic motions in the equatorial area. *J. Meteorol. Soc. Jpn.* 44, 25–43. https://doi.org/10.2151/jmsj1965.44.1_25.
- Neale, R.B., Richter, J., Park, S., Lauritzen, P.H., Vavrus, S.J., Rasch, P.J., Zhang, M.H., 2013. The mean climate of the community atmosphere model (CAM4) in forced SST and fully coupled experiments. *J. Clim.* 26, 5150–5168. <https://doi.org/10.1175/JCLI-D-12-00236.1>.
- Rao, Z., Wu, D., Shi, F., Guo, H., Cao, J., Chen, F., 2019. Reconciling the ‘westerlies’ and ‘monsoon’ models: a new hypothesis for the Holocene moisture evolution of the Xinjiang region, NW China. *Earth Sci. Rev.* 191, 263–272. <https://doi.org/10.1016/j.earscirev.2019.03.002>.
- Rashid, H., Flower, B.P., Poore, R.Z., Quinn, T.M., 2007. A ~25 ka Indian Ocean monsoon variability record from the Andaman Sea. *Quat. Sci. Rev.* 26, 2586–2597. <https://doi.org/10.1016/j.quascirev.2007.07.002>.
- Sato, T., Kimura, F., 2005. Impact of diabatic heating over the Tibetan Plateau on subsidence over northeast Asian arid region. *Geophys. Res. Lett.* 32, L05809. <https://doi.org/10.1029/2004GL022089>.
- Schiemann, R., Lüthi, D., Schär, C., 2009. Seasonality and interannual variability of the westerly jet in the Tibetan plateau region. *J. Clim.* 22, 2940–2957. <https://doi.org/10.1175/2008JCLI2625.1>.
- Schilt, A., Baumgartner, M., Blunier, T., Schwander, J., Spahni, R., Fischer, H., Stocker, T.F., 2010. Glacial-interglacial and millennial-scale variations in the atmospheric nitrous oxide concentration during the last 800,000 years. *Quat. Sci. Rev.* 29, 182–192. <https://doi.org/10.1016/j.quascirev.2009.03.011>.
- Shapiro, M.A., 1982. Mesoscale weather systems of the Central United States. (Tech. Rep. 3.1-77). In: The National STORM Program: Scientific and Technological Bases and Major Objectives. University Corporation for Atmospheric Research.
- Shi, Z., Zhou, P., Li, X., Cheng, H., Sha, Y., Xie, X., Liu, H., Wu, J., Liu, X., 2021. Distinct Holocene precipitation trends over arid Central Asia and linkages to westerlies and Asian monsoon. *Quat. Sci. Rev.* 266, 107055. <https://doi.org/10.1016/j.earscirev.2021.107055>.
- Song, F., Leung, L.R., Lu, J., Dong, L., 2018. Future changes in seasonality of the North Pacific and North Atlantic subtropical highs. *Geophys. Res. Lett.* 45, 11,959–11,968. <https://doi.org/10.1029/2018GL079940>.
- Sun, H., Liu, X., 2021. Impacts of dynamic and thermal forcing by the Tibetan Plateau on the precipitation distribution in the Asian arid and monsoon regions. *Clim. Dyn.* 56, 2339–2358. <https://doi.org/10.1007/s00382-020-05593-9>.

- Wang, W., Feng, Z., 2013. Holocene moisture evolution across the Mongolian Plateau and its surrounding areas: a synthesis of climatic records. *Earth Sci. Rev.* 122, 38–57. <https://doi.org/10.1016/j.earscirev.2013.03.005>.
- Wang, W., Feng, Z., Ran, M., Zhang, C., 2013. Holocene climate and vegetation changes inferred from pollen records of Lake Aibi, northern Xinjiang, China: a potential contribution to understanding of Holocene climate pattern in East-central Asia. *Quat. Int.* 311, 54–62. <https://doi.org/10.1016/j.quaint.2013.07.034>.
- Wang, N., Jiang, D., Lang, X., 2020. Seasonality in the response of East Asian westerly jet to the mid-Holocene forcing. *J. Geophys. Res. Atmos.* 125, e2020JD033003. <https://doi.org/10.1029/2020JD033003>.
- Wang, Y.V., Larsen, T., Lauterbach, S., Andersen, N., Blanz, T., Krebs-Kanzow, U., Gierz, P., Schneider, R.R., 2022. Higher sea surface temperature in the Indian Ocean during the last interglacial weakened the South Asian monsoon. *Proc. Natl. Acad. Sci. USA* 119, e2107720119. <https://doi.org/10.1073/pnas.2107720119>.
- Wang, S., Huang, J., Huang, G., Luo, F., Ren, Y., He, Y., 2022a. Enhanced impacts of Indian Ocean Sea surface temperature on the dry/wet variations over Northwest China. *J. Geophys. Res. Atmos.* 127, e2022JD036533. <https://doi.org/10.1029/2022JD036533>.
- Wang, T., Xu, H., Jiang, D., Yao, J., 2022b. Mechanisms of reduced mid-holocene precipitation in arid Central Asia as simulated by PMIP3/4 models. *J. Geophys. Res. Atmos.* 127, e2021JD036153. <https://doi.org/10.1029/2021JD036153>.
- Wanner, H., Beer, J., Bütkofer, J., Crowley, T.J., Cubasch, U., Flückiger, J., Goosse, H., Grosjean, M., Joos, F., Kaplan, J.O., Küttel, M., Müller, S.A., Prentice, I.C., Solomina, O., Stocker, T.F., Tarasov, P., Wagner, M., Widmann, M., 2008. Mid- to Late Holocene climate change: an overview. *Quat. Sci. Rev.* 27, 1791–1828. <https://doi.org/10.1016/j.quascirev.2008.06.013>.
- Wu, G., Duan, A., Liu, Y., Mao, J., Ren, R., Bao, Q., He, B., Liu, B., Hu, W., 2015. Tibetan Plateau climate dynamics: recent research progress and outlook. *Natl. Sci. Rev.* 2, 100–116. <https://doi.org/10.1093/nsr/nwu045>.
- Wu, P., Liu, Y., Ding, Y., Li, X., Wang, J., 2022. Modulation of sea surface temperature over the North Atlantic and Indian-Pacific warm pool on interdecadal change of summer precipitation over Northwest China. *Int. J. Climatol.* 42, 8526–8538. <https://doi.org/10.1002/joc.7743>.
- Xu, H., Zhou, K., Lan, J., Zhang, G., Zhou, X., 2019. Arid Central Asia saw mid-Holocene drought. *Geology* 47, 255–258. <https://doi.org/10.1130/G45686.1>.
- Yang, J., Li, G., Gan, Y., Chen, Z., Zhang, X., 2023. Role of the tropical Indian Ocean in orbitally induced mid-Holocene precipitation variation in Northwest China. *Quat. Sci. Rev.* 317, 108285. <https://doi.org/10.1016/j.quascirev.2023.108285>.
- Zhang, X., 2021. Penetration of monsoonal water vapour into arid Central Asia during the Holocene: an isotopic perspective. *Quat. Sci. Rev.* 251, 106713. <https://doi.org/10.1016/j.quascirev.2020.106713>.
- Zhang, X., Jin, L., 2016. Association of the Northern Hemisphere circumglobal teleconnection with the Asian summer monsoon during the Holocene in a transient simulation. *Holocene* 26, 290–301. <https://doi.org/10.1177/0959683615608689>.
- Zhang, X., Jin, L., Chen, J., Chen, F., Park, W., Schneider, B., Latif, M., 2017. Detecting the relationship between moisture changes in arid Central Asia and East Asia during the Holocene by model-proxy comparison. *Quat. Sci. Rev.* 176, 36–50. <https://doi.org/10.1016/j.quascirev.2017.09.012>.
- Zhang, J., Huan, X., Lü, H., Wang, C., Shen, C., He, K., Lü, Y., Wu, N., 2022a. Crossing of the Hu line by Neolithic population in response to seesaw precipitation changes in China. *Sci. Bull.* 67, 844–852. <https://doi.org/10.1016/j.scib.2021.12.011>.
- Zhang, X., Chen, C., Zhao, W., Jin, L., 2022b. Role of Asian westerly jet core's zonal migration in holocene East Asian summer monsoon precipitation. *J. Geophys. Res. Atmos.* 127, e2021JD036179. <https://doi.org/10.1029/2021JD036179>.
- Zhang, X., Liu, B., Chen, S., Fu, Z., Xie, T., Chen, F., 2022c. Increased water vapor supply in winter and spring leading to the arid Central Asian wetting in last 6000 years. *Sci. China Earth Sci.* 65, 1353–1367. <https://doi.org/10.1007/s11430-021-9921-7>.
- Zhang, X., Chen, C., Zhao, W., 2023. Remote insolation forcing of orbital-scale South Asian summer monsoon variability. *Geophys. Res. Lett.* 50, e2023GL105003. <https://doi.org/10.1029/2023GL105003>.
- Zhang, X., Chen, C., Zhao, W., 2024. Influence of equatorial spring insolation on abrupt Asian summer monsoon decline at orbital scale. *J. Geophys. Res. Atmos.* 129, e2024JD040816. <https://doi.org/10.1029/2024JD040816>.
- Zhou, T., Yu, R., Zhang, J., Drange, H., Cassou, C., Deser, C., Hodson, D.L.R., SanchezGomez, E., Li, J., Keenlyside, N., Xin, X., Okumura, Y., 2009. Why the western Pacific subtropical high has extended westward since the late 1970s. *J. Clim.* 22, 2199–2215. <https://doi.org/10.1175/2008JCLI2527.1>.